

Article

A Control Strategy of *LCL*-Type Grid-Connected Inverters for Improving the Stability and Harmonic Suppression Capability

Xian Wang ^{1,2}, Dazhi Wang ^{1,*} and Shuai Zhou ¹¹ School of Information Science & Engineering, Northeastern University, Shenyang 110819, China² Northeast Branch of State Grid Corp., Shenyang 110180, China

* Correspondence: wangdazhi@ise.neu.edu.cn or prozdw@126.com

Abstract: The conventional inverter-side current single-loop feedback control scheme is weak in suppressing the grid-side current harmonics, posing a challenge for an inverter to inject high-quality current under distorted grid voltage. With capacitor current compensation added, the control scheme achieves controllability of the grid-side current harmonics so that it can effectively suppress some specific harmonic components. However, due to the stability requirements, only a few low-order harmonic resonance controllers can be applied, which limits the mitigation of high-order harmonics. To tackle this problem, the grid-side current feedback control with inductor–capacitor–inductor (*LCL*) resonance damping is proposed in this paper. In this case, a higher *LCL* resonance frequency can be set compared to the inverter-side current single-loop feedback control scheme. Thereby, more resonance controllers can be applied to suppress high-order grid-side current harmonics. The active damping method of capacitor current proportional feedback plus capacitor voltage proportional feedback is adopted because of its high robustness to grid impedance variations. Furthermore, this paper reveals that the applied active damping method has a limitation in that it only considers a single inverter under inductive grid impedance, which cannot eliminate the risk of resonance caused by the interaction of multiple inverters and the grid. To address this issue, a phase lead compensator (PLC) is proposed, eliminating the resonance risk by removing the non-passive region of the inverter output admittance. To retain the advantage of the inverter-side current single-loop feedback control scheme, i.e., only a few measuring devices are required, a digital differentiator is used to calculate the capacitor current from the capacitor voltage. The difference between the measured inverter-side current and the calculated capacitor current is taken to approximate the grid-side current for the feedback control. The control performance is comparable to using the grid-side current for feedback. Simulation and experimental results demonstrate that the proposed control scheme endows the inverter with good stability and current quality without extra measurement devices.

Keywords: *LCL* filter; current control; resonance damping; harmonic suppression; passivity; stability

Citation: Wang, X.; Wang, D.; Zhou, S. A Control Strategy of *LCL*-Type Grid-Connected Inverters for Improving the Stability and Harmonic Suppression Capability. *Machines* **2022**, *10*, 1027. <https://doi.org/10.3390/machines10111027>

Academic Editors: Paula Bastida-Molina, Raquel Villena-Ruiz and Andres Honrubia-Escribano

Received: 16 September 2022

Accepted: 1 November 2022

Published: 4 November 2022

Publisher's Note: MDPI stays neutral with regard to jurisdictional claims in published maps and institutional affiliations.



Copyright: © 2022 by the authors. Licensee MDPI, Basel, Switzerland. This article is an open access article distributed under the terms and conditions of the Creative Commons Attribution (CC BY) license (<https://creativecommons.org/licenses/by/4.0/>).

1. Introduction

In a renewable energy generation system, grid-connected pulse-width modulation (PWM) inverters play a significant role in connecting renewable energy to the utility grid. Compared with the *L* filter, the *LCL* filter has an excellent high-frequency harmonic attenuation performance with a smaller volume, making it a common solution for filtering harmonics produced by the PWM inverter [1]. However, two problems have to be faced with an *LCL* filter. One is the *LCL* resonance, which may challenge the stability of the inverter control system [2]. Assume the total delay time is $1.5T_s$ for the digital calculation and PWM process. T_s represents the sampling period [3]. For the inverter-side current single-loop feedback control, the stable region of *LCL* resonant frequency f_r is $(0, f_s/6)$, and the unstable region is $(f_s/6, f_s/2)$. f_s is the sampling frequency. $f_s/6$ is the critical frequency that divides the stable and unstable regions. For the grid-side current single-loop feedback control, the stability region is divided exactly the opposite way to the former. When the

LCL resonant frequency is in the corresponding stable region and the current regulator parameters are reasonably designed, the inverter-side or the grid-side current single-loop feedback control can enable an inverter to operate stably [4]. With the grid impedance changes, the actual resonant frequency will vary widely and may enter the unstable region, making the system unstable [5]. Therefore, many stability enhancement methods such as active damping based on filters [6,7], state variable feedback [8–12], delay time control [1,4] and some resonance analysis studies [13,14] have been proposed in recent years. Another problem is that compared with the *L* filter, the total inductance employed by the *LCL* filter is smaller. As a result, the grid voltage harmonics are more likely to distort the current injected into the grid by the inverter [15]. The multi-resonant regulators in the stationary frame [16,17], proportional–integral (PI) regulators [18] in the multi-synchronous reference frames or grid voltage feedforward [19,20] are the common choice to solve this problem. For most inverter products, a group of current sensors is set to measure the inverter-side current, providing overcurrent protection for the inverter [21]. Compared with the grid-side current feedback control, the inverter-side current feedback control is cost-saving since it does not require the grid-side current sensors [15]. However, the grid-side current is not directly controlled, which may leave it distorted. This issue can be tackled by adding harmonic information to the inverter-side reference current [15,22], but no *LCL* resonance damping applied will result in a strong interaction between the frequency characteristics of the *LCL* resonance and those around the resonance controller. To mitigate its effect on stability, the resonance frequencies of the resonance controllers should be much lower than that of the *LCL* filter [23]. The inverter-side current single-loop feedback control requires an *LCL* resonant frequency below $f_s/6$, which further limits the application of high-order resonant controllers. The grid-side current single-loop feedback control permits setting the *LCL* resonant frequency in $(f_s/6, f_s/2)$. Accordingly, the application range of resonant controllers is extended, but as the grid impedance increases, the *LCL* resonant frequency may enter the instability region of $(0, f_s/6)$, causing system instability [5]. To improve the robust stability against grid impedance changes, this paper suggests the grid-side current feedback control with the damping method as proportional feedback of capacitor current plus proportional feedback of capacitor voltage, for which the maximum allowable *LCL* resonant frequency is close to the Nyquist frequency [24], allowing for more high-order harmonic resonance controllers to be incorporated, further improving the quality of the injected current. Additionally, the damping method has high robustness to the variation of the grid equivalent inductance or the *LCL* filter parameters. However, it is only studied for a single inverter under inductive grid impedance. Further analysis is needed for its applicability in more complex situations.

With the development of renewable energy, more and more inverters are connected to the grid, making the system increasingly complex [25]. The interaction among multiple inverters, reactive power compensation devices, loads and transmission lines may cause the system to resonate at various frequencies. Enabling each inverter to meet internal stability (considering the inverter itself) and external stability (considering the overall system) can eliminate the risk of resonance [26]. For the adopted method, internal stability is well satisfied [24]. External stability is determined by the output admittance of the inverter, as it reflects the external characteristics of the inverter. External stability can be assessed according to the frequency-domain passivity theory [27]. A system is stable if each component is passive [28]. The grid admittance is generally passive. Therefore, the system stability can be guaranteed if the output admittance of each inverter in the system is passive. The inverter output admittance Y_o is passive if it satisfies the following two conditions: (1) Y_o has no right-half-plane pole, (2) the real part of Y_o is non-negative in the controllable frequency range, i.e., $[0, f_s/2]$ [29]. Condition 1 also implies that an inverter can operate stably if the influence of the other components in the system is negligible, which corresponds to internal stability. Condition 2 corresponds to external stability [29]. Reference [28] proposed a passive enhancement method for inverters with single-loop feedback control, which cannot guarantee the output admittance passive throughout the controllable frequency range.

Reference [26] proposed a passive enhancement method for inverters with grid-side current feedback control and capacitor current feedback active damping, which requires a proper selection of *LCL* filter parameters to prevent the *LCL* resonant frequency from entering the unstable region. In this paper, the adopted active damping method [24] can almost eliminate the unstable region of the *LCL* resonant frequency, making it easier to design the *LCL* filter parameters than in [26].

This paper reveals that for the method proposed in [24], the real part of Y_o is negative above a certain frequency, implying the existence of a non-passive admittance region. In this case, *LC* resonance may be generated between the inverter output admittance and the equivalent grid admittance [28], indicating system instability. To eliminate the non-passive region of Y_o , this paper proposes to insert a phase lead compensator (PLC) cascaded in series with the current regulator. In this way, the inverter satisfies internal and external stability over the entire controllable frequency range.

The proposed scheme improves the grid-side current quality with enhanced system stability, which requires the grid-side current for feedback control and the capacitor current for active damping. It is preferable to avoid investments in the corresponding measurement devices, which leads to the development of the sensorless methods [30–32]. This paper calculates the capacitor current from the capacitor voltage measured for the phase-locked loop (PLL). The estimated capacitor current is subtracted from the measured inverter-side current, by which the approximate grid-side current can be obtained. Through the above method, the applied measurement devices are identical to that of the inverter-side current single-loop feedback control scheme, retaining the latter's advantage that only a few measurement devices are required.

The rest of this paper is organized as follows. Section 2 revisits the inverter-side current single-loop feedback control with capacitor current compensation, unveiling that the restriction on *LCL* resonant frequency results in limited improvement in harmonic suppression. Section 3 reveals the presence of a non-passive region with the adopted damping method, which can be eliminated by the proposed PLC, and illustrates that special care should be taken when using the calculated capacitor current for active damping. Section 4 investigates the effectiveness of the PLC in improving external stability through a case study. Section 5 demonstrates the excellent harmonic suppression capability of the proposed method. Section 6 verifies the theoretical analysis through simulations and experiments. Section 7 concludes this paper.

2. Problem Formulation for Current Single-Loop Feedback Control

2.1. System Description

Figure 1a shows the single-phase equivalent circuit of a three-phase balanced wind power generation system. A permanent magnet synchronous generator (PMSG) is connected to the grid through a back-to-back dual-PWM converter. Replacing the DC side with other renewable energy sources does not affect the analytical conclusions. The grid-side inverter is connected to the grid through an *LCL* filter composed of the inverter-side inductor L_1 , the filter capacitor C_f and the grid-side inductor L_2 . L_g is the grid inductor. i_{L1} , i_c , i_{L2} , v_c , v_g and V_{in} are the inverter-side current, the capacitor current, the grid-side current, the measured capacitor voltage, the grid voltage and the DC-link voltage, respectively.

The current control is implemented in the $\alpha\beta$ reference frame. The current regulator consists of a proportional controller, several quasi-resonant controllers for reference tracking and selective harmonic suppression [33], expressed as

$$G_i(s) = K_p + \sum_{h=1}^M K_{ih} \frac{s \cdot \cos(\theta_h) - \omega_h \cdot \sin(\theta_h)}{s^2 + \omega_h^2} \quad (1)$$

where K_p is the proportional gain, ω_h is the angular frequency at $h\omega_0$, ω_0 is the fundamental angular frequency, h is the harmonic order, K_{ih} is the resonant gain at ω_h , M is the maximum order of the quasi-resonant controller and θ_h ($h = 1, 2, \dots, M$) is the phase lead for mitigating

the h th-order resonant controller's effect on the phase margin, which helps to extend the harmonic suppression range of the current regulator from below the open-loop crossover frequency to approach the LCL resonant frequency [23].

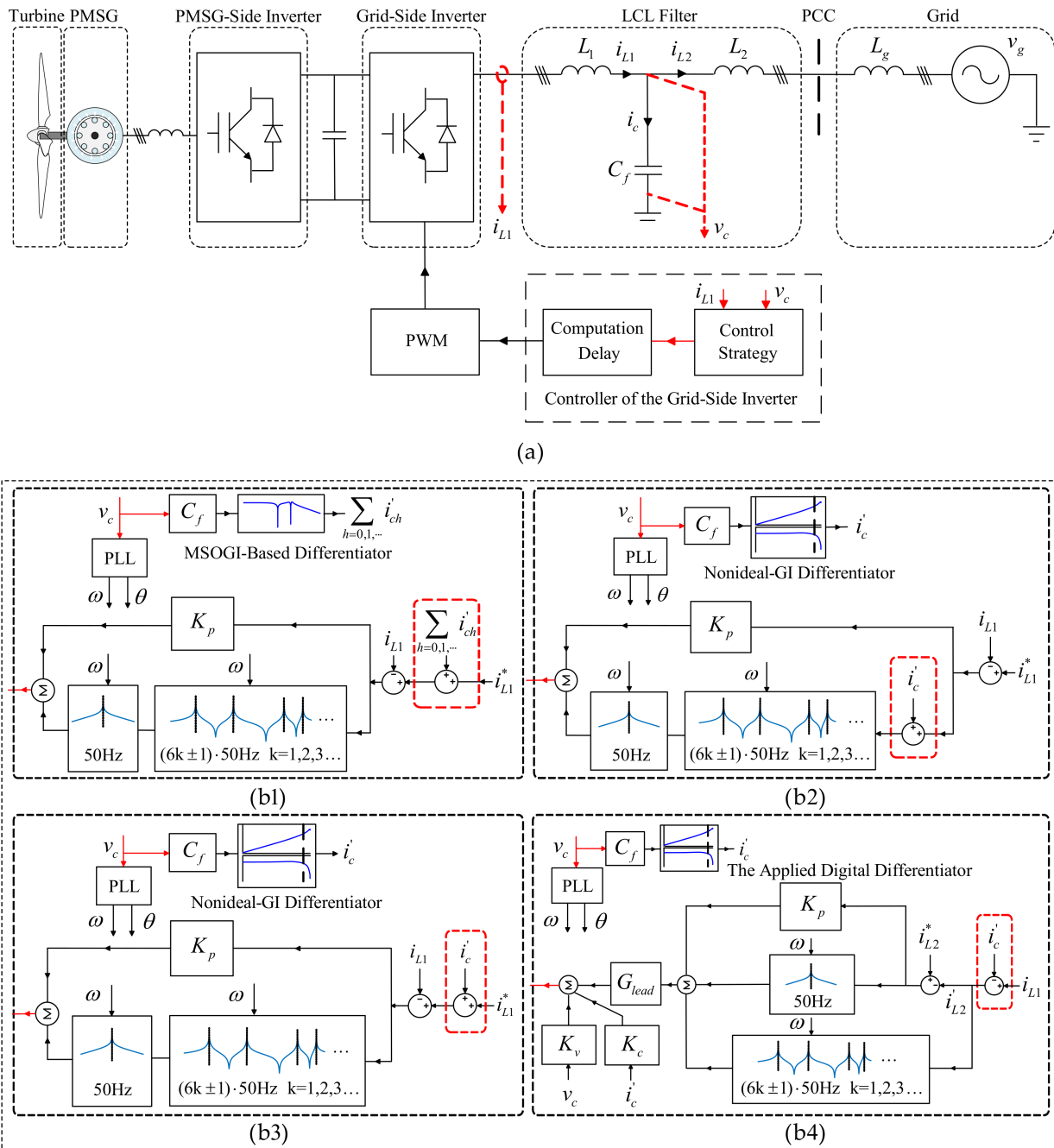


Figure 1. A three-phase balanced wind power generation system: (a) Single-phase equivalent circuit; (b1–b4) control block diagrams of the grid-side inverter.

2.2. Analysis of the Harmonic Suppression Capability under the Single-Loop Feedback Control

The current injected into the grid should comply with relevant standards, such as [34], which specify the allowable harmonic current injected into the grid. For the conventional inverter-side current single-loop feedback control, the inverter-side current is taken as the controlled object. Since the inverter-side reference current contains only fundamental components, the resonant controllers can only effectively suppress the harmonic components at

the inverter-side rather than that at the grid-side, which may make the grid-side current fail to meet relevant requirements.

2.2.1. The Improved Inverter-Side Current Single-Loop Feedback Control

Adding the capacitor current harmonic information to the inverter-side reference current can directly suppress the grid-side current harmonics [15,22]. Figure 1b1 extracts the capacitor current harmonics from the capacitor voltage using multiple differentiators based on second-order generalized integrators [22]. Figure 1b2 calculates the capacitor current from the capacitor voltage using non-ideal generalized integrator derivatives. The calculated capacitor current is then added to the harmonic resonance controllers' branch, from which the harmonic information of the capacitor current can be obtained [15]. Incorporating the harmonic information into the inverter-side current reference value results in the inverter-side current containing the $6k \pm 1$ th order harmonics of the capacitor current, $k = 1, 2, \dots, M$, which indicates that the harmonic currents will flow through the L_1 – C_f current loop instead of the L_2 – C_f current loop, making the grid-side current free of them. However, the improvement on the grid-side current is limited. First, the methods in [15,22] are equivalent to the grid-side current single-loop feedback control for only specific resonant frequencies, while for other frequencies, they are still equal to the inverter-side current single-loop feedback control. In addition, only a handful of resonance controllers can be used due to the limitation of the relatively low LCL resonant frequency. The usage of resonance controllers is further restricted when the LCL resonant frequency decreases as the grid inductance increases. Taking the method in [15] as the analysis object, the LCL parameters in this section are set as follows: $L_1 = 860 \mu\text{H}$, $L_2 = 90 \mu\text{H}$ and $C_f = 230 \mu\text{F}$. Only C_f differs from the corresponding value in Table 1. The parameters are set in this way to make the frequency characteristic close to that of [15] and to facilitate the comparison with the proposed scheme. The initial resonant frequency of an LCL filter is expressed as

$$f_{r0} = \frac{1}{2\pi} \sqrt{\frac{L_1 + L_2}{L_1 \cdot L_2 \cdot C_f}} \quad (2)$$

Table 1. Parameters of the main circuit and the controller.

Parameters	Value	Parameters	Value
Grid voltage V_g/V	220	Resonant frequency f_{r_pro}/Hz	2788
Grid fundamental frequency f_0/Hz	50	Current sensor gains H_i, H_{i2}	0.15
Inverter DC-link voltage V_{in}/V	360	Feeder inductance $L_c/\mu\text{H}$	196
Amplitude of the triangular carrier V_{tri}/V	4.58	Feeder capacitance $C_c/\mu\text{F}$	0.24
Sampling frequency f_s/kHz	20	Load equivalent capacitance $C_{load}/\mu\text{F}$	0.6
LCL —Inverter-side inductor $L_1/\mu\text{H}$	860	Proportional gain K_p	0.405
LCL —Grid-side inductor $L_2/\mu\text{H}$	90	hth resonator gain K_{ih}	32
LCL —Capacitor $C_f/\mu\text{F}$	5	Capacitor current feedback coefficient H_{i1}	−0.06
Resonant frequency f_{r0_inv}/Hz	1163	Capacitor voltage feedback coefficient K	−1600
Resonant frequency f_{r_inv}/Hz	411	Lead compensator factor α_{lead}	1.42
Resonant frequency f_{r0_pro}/Hz	7885	Lead compensator factor τ_{lead}	4×10^{-5}

When the grid inductance $L_g = 0$, taking the above LCL parameters into (2), the initial resonant frequency is obtained as $f_{r0_inv} \approx 1163 \text{ Hz}$. When L_g increases to 10% per unit, i.e., 2.6 mH [24], replacing L_2 in (2) with $L_T = L_2 + L_g$, the actual resonant frequency is obtained as $f_{r_inv} \approx 411 \text{ Hz}$.

Figure 2 displays a series of equivalent control block diagrams of Figure 1b2, in which Figure 2a is successively simplified to Figure 2b–d. To make the transformation process concise, the grid voltage is first omitted.

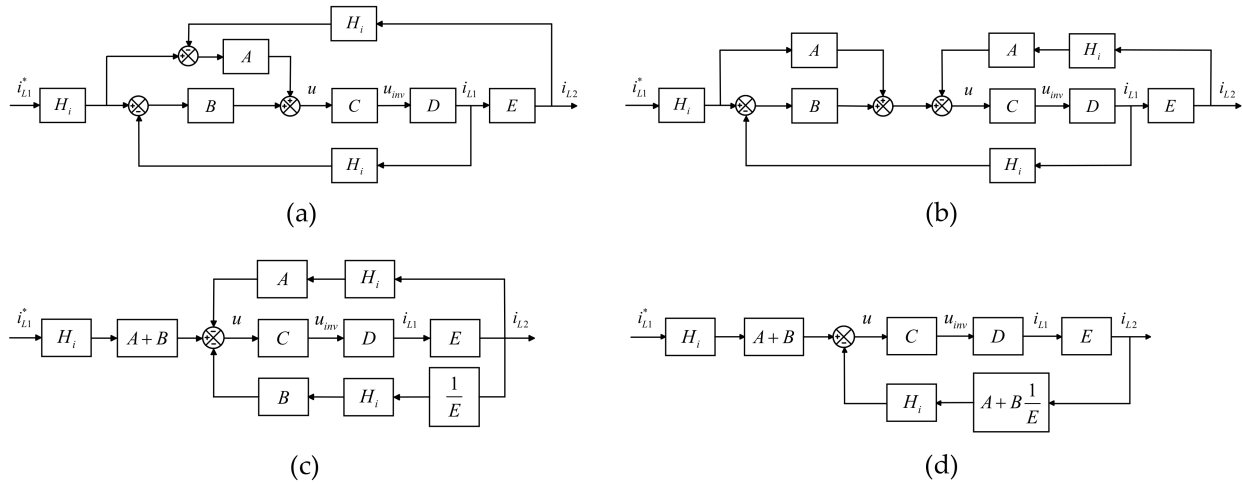


Figure 2. The equivalent control block diagrams of Figure 1b2: (a) The original one; (b–d) The simplified ones.

In Figure 2a, H_i represents the sensor gain for both currents at the grid side and at the inverter side, A represents the harmonic resonance controller, B represents the proportional controller plus the fundamental resonance controller, C represents the transfer function from the current regulator output u to the inverter output voltage u_{inv} , composed of the control delay, i.e., $1.5T_s$ and the inverter gain K_{pwm} , D represents the transfer function from inverter output voltage u_{inv} to the inverter-side current i_{L1} , E represents the transfer function from the inverter-side current i_{L1} to the grid-side current i_{L2} . A , B , C , D and E are expressed in order as

$$A = \sum_{h=2}^M K_{ih} \frac{s \cdot \cos(\theta_h) - \omega_h \cdot \sin(\theta_h)}{s^2 + \omega_h^2}, \quad (3)$$

$$B = K_p + K_{i1} \frac{s \cdot \cos(\theta_1) - \omega_1 \cdot \sin(\theta_1)}{s^2 + \omega_1^2}, \quad (4)$$

$$C = e^{-1.5sT_s} \cdot K_{PWM}, \quad (5)$$

$$D = \frac{1}{L_1 L_T C_f} \cdot \frac{L_T C_f s^2 + 1}{s(s^2 + \omega_{res}^2)}, \quad (6)$$

$$E = \frac{1}{L_T C_f s^2 + 1}. \quad (7)$$

2.2.2. Closed-Loop Response Analysis

The block diagram in Figure 2d is redrawn in Figure 3a1 for easy visibility. From Figure 3a1, the grid-side current i_{L2} is derived as

$$i_{L2}(s) = G_{cl}(s) i_{L1}^*(s) \quad (8)$$

where $G_{cl}(s)$ denotes the closed-loop transfer function of the inverter-side current reference value i_{L1}^* to i_{L2} , expressed as

$$G_{cl}(s) = \frac{H_i(A+B)CDE}{1 + H_i(DA+B)CE}. \quad (9)$$

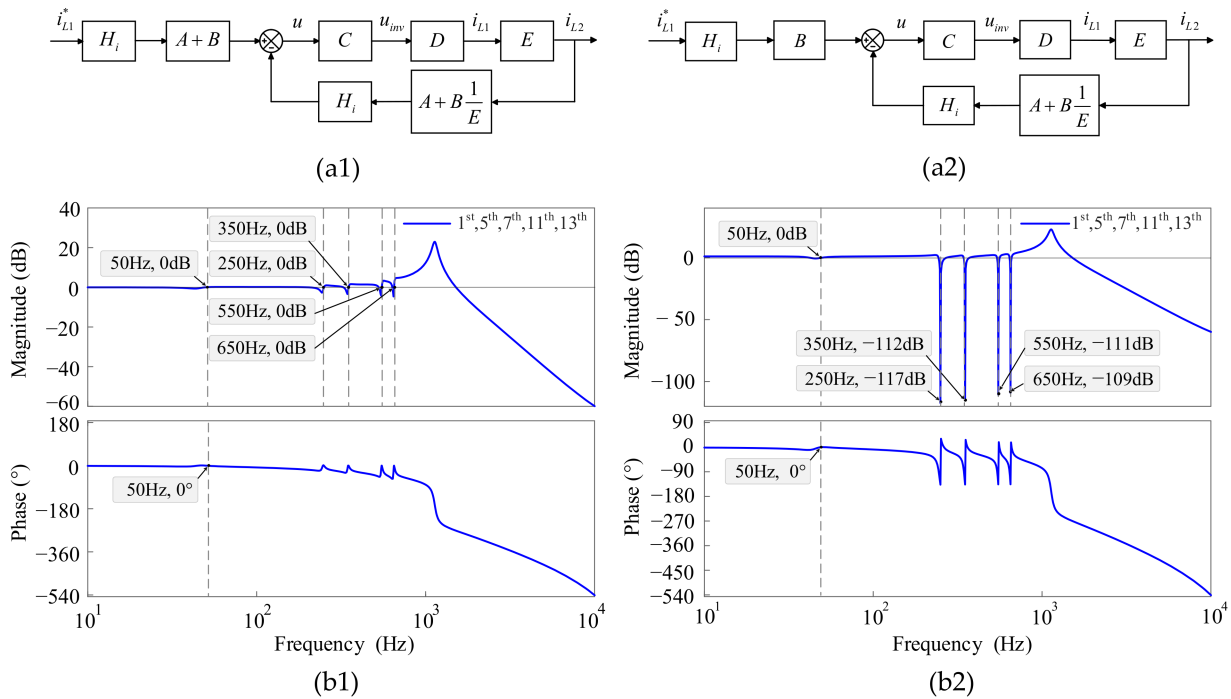


Figure 3. Control block diagrams and the corresponding closed-loop Bode plots: (a1,b1) The original ones; (a2,b2) the improved ones.

The Bode plot of $G_{cl}(s)$ is given in Figure 3b1, in which the amplitudes at the characteristic harmonic frequencies are all close to 0 dB, indicating that the original method cannot suppress the characteristic harmonics induced by the reference current. When disconnecting the path from the grid-side current reference $i_{L1}^*(s)$ through controller A to the controller output u , the corresponding control block diagram is redrawn in Figure 3a2. The grid-side current i_{L2} is expressed as

$$i_{L2}(s) = G'_{cl}(s)i_{L1}^*(s) \quad (10)$$

where $G'_{cl}(s)$ is the corresponding closed-loop transfer function from i_{L1}^* to i_{L2} , expressed as

$$G'_{cl}(s) = \frac{H_i B C D E}{1 + H_i (D A + B) C E}. \quad (11)$$

Figure 3b2 shows the Bode plot of $G'_{cl}(s)$, indicating that the characteristic harmonics brought by i_{L1}^* can be effectively suppressed. Figure 4a shows the Bode plots of $G'_{cl}(s)$ when different numbers of harmonic resonance controllers are used. The amplitude–frequency response of $G'_{cl}(s)$ has a spike around the LCL resonance frequency, which will increase as more resonance controllers are applied. During the inverter startup or when the reference current undergoes a step change, the harmonic components around the spike frequency will appear in the reference current and be amplified in the grid-side current.

2.2.3. Open-Loop Response Analysis

The open-loop transfer function can be obtained from Figure 3a2 as

$$G_{ol}(s) = C D (A E + B) H_i. \quad (12)$$

When $L_g = 0$, the 5th, 7th, 11th and 13th harmonic resonance controllers are inserted. Figure 4b shows the Bode plot of $G_{ol}(s)$. The phase margin PM_1 is 55.6° , and the gain margin GM_1 is 11.4 dB. Both of them satisfy the stability margin requirements in classical control theory: $PM \in (30^\circ, 60^\circ)$, $GM \geq 3\text{--}6$ dB. Figure 5a shows the Bode plot of $G_{ol}(s)$

after the 17th order resonance controller is inserted. One positive crossing occurs near the 17th harmonic frequency, while no negative crossing occurs. Moreover, the open-loop transfer function $G_{ol}(s)$ has no right-half-plane pole. According to the Nyquist stability criterion, the closed-loop transfer function $G_{cl}'(s)$ has a pair of right-half-plane poles, which indicates that the system is unstable. To leave a sufficient gain margin, harmonic resonance controllers' usage is further limited. Figure 5b shows the corresponding open-loop Bode plot with only the 5th order resonant controller inserted when L_g increases to 10% per unit, i.e., 2.6 mH [24]. One negative crossing occurs near the 5th harmonic frequency, while no positive crossing occurs. Moreover, the open-loop transfer function has no right-half-plane pole. Similar to the previous analysis, the system is unstable, which indicates that the stability of the resonance controllers will be affected by the LCL resonance if it is not properly damped. For this reason, resonant controllers are usually set below the open-loop crossover frequency [2,35].

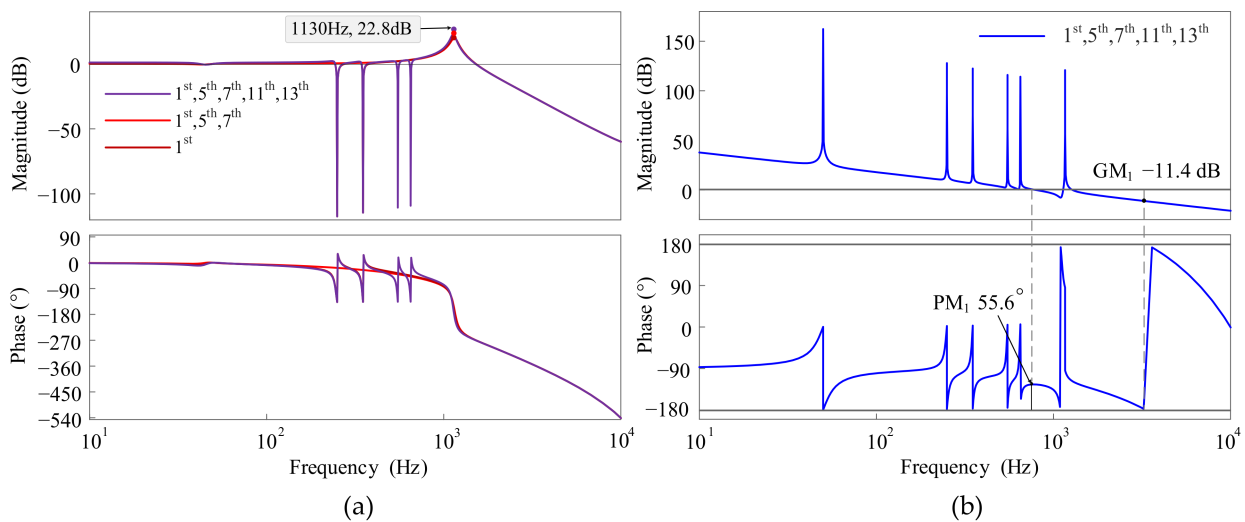


Figure 4. Bode plots of the corresponding transfer functions: (a) Bode plots of the closed-loop transfer function $G_{cl}'(s)$ when different numbers of resonance controllers are used; (b) Bode plot of the open-loop transfer function $G_{ol}(s)$ when $L_g = 0$.

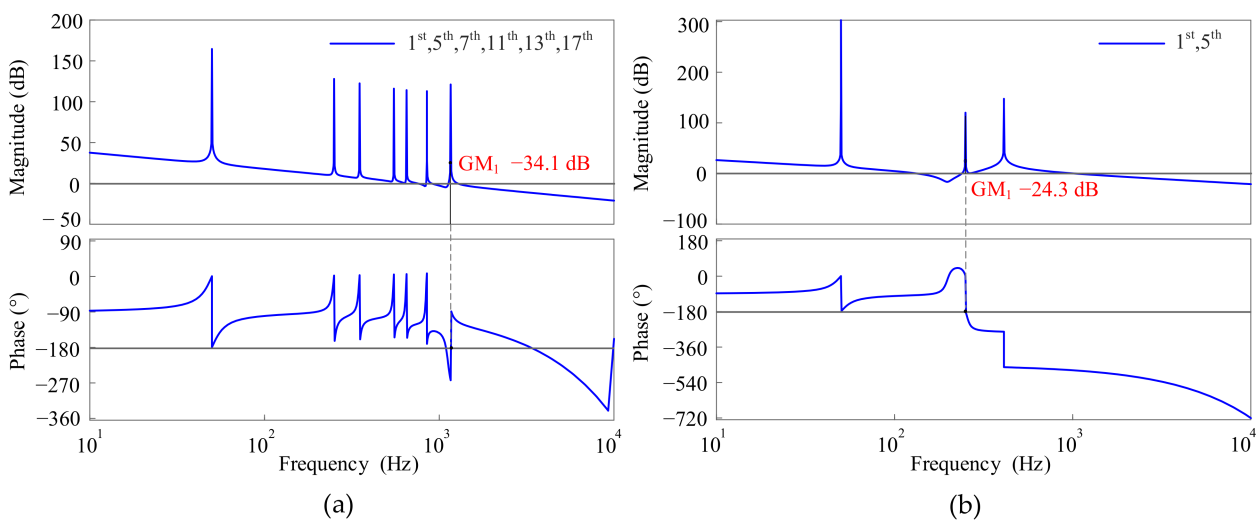


Figure 5. Bode plots of the open-loop transfer function $G_{ol}(s)$: (a) $L_g = 0$, with the 1st, 5th, 7th, 11th, 13th and 17th resonance controller applied; (b) $L_g = 2.6$ mH, with the 1st, 5th resonance controller applied.

2.2.4. Harmonic Suppression Analysis

Figure 6a shows the control block diagram for analyzing the effect of the grid voltage v_g . F is the open-loop transfer function from v_g to i_{L2} , denoted as

$$F = \frac{L_T C_f s^2 + 1}{L_1 L_T C_f s^3 + (L_1 + L_T) s}. \quad (13)$$

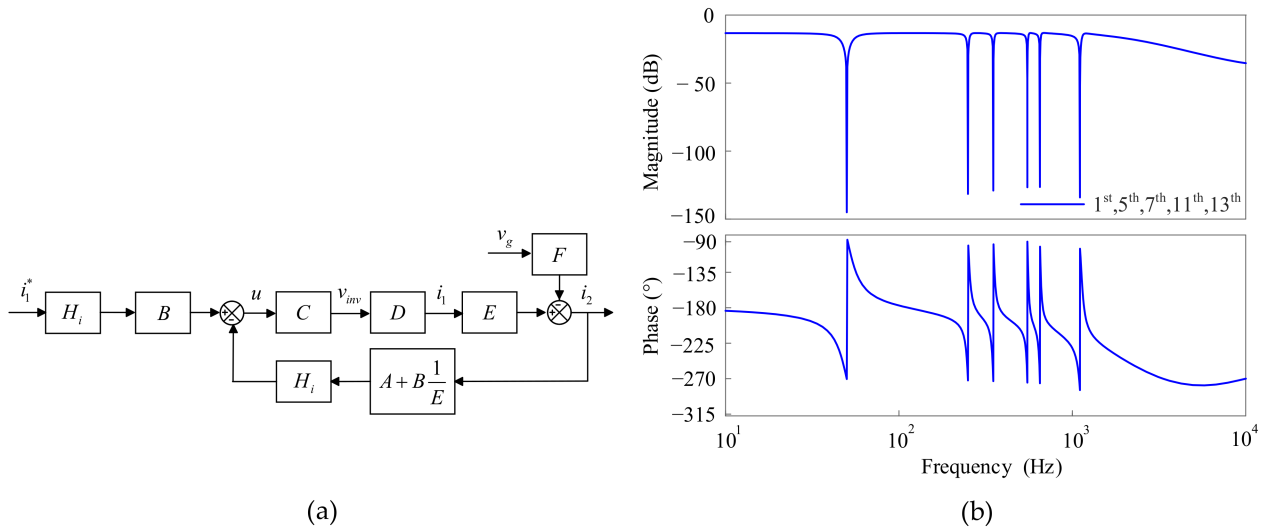


Figure 6. Analysis of the effects of the grid voltage: (a) Control block diagram; (b) Bode plot of the closed-loop transfer function $G_{vcl}(s)$ when $L_g = 0$.

The closed-loop transfer function from v_g to i_{L2} can be derived from Figure 6a as

$$G_{vcl}(s) = -\frac{F}{1 + CD(AE + B)H_i}. \quad (14)$$

Figure 6b shows the Bode plot of $G_{vcl}(s)$, which illustrates that the grid-side current can be free from the 1st, 5th, 7th, 11th and 13th order components of the grid voltage.

2.2.5. Simulation Verification

To verify the above analysis, a set of simulations are performed with MATLAB/Simulink.

Simulation 1: Set $L_g = 0$. The inverter-side current reference value i_{L1}^* jumps from 30 A to 40 A at 0.225 s and from 40 A back to 30 A after 0.08 s. The voltage source contains $6k \pm 1$ order harmonic voltage with an amplitude of 30 V, where $k = 1, 2$. Harmonic resonance controllers of the corresponding orders are inserted. Figure 7a,b show the grid-side current waveform and its fast Fourier transform (FFT) analysis result, respectively. In Figure 7a, during the half fundamental period after i_{L1}^* jumps, the grid-current is seriously distorted, which is caused by the harmonics around the spike frequency. Due to the space limitation, the FFT analysis result is not presented. After half a fundamental cycle, the grid-side current distortion basically disappears. An FFT analysis is performed on the periodic waveform marked red in Figure 7a, and the results are shown in Figure 7b. The total harmonic distortion (THD) of i_{L2} is 1.64%, which proves that the resonance controllers can effectively suppress the $6k \pm 1$ order harmonics, where $k = 1, 2$.

Simulation 2: Set $L_g = 0$, the inverter-side reference current $i_{L1}^* = 30 \sin \omega_0 t$ A. The voltage source contains harmonic components of the 5th, 7th, 11th, 13th and 17th orders with an amplitude of 30 V. Harmonic resonance controllers with the corresponding orders are used. Figure 8a,b show the grid-side current waveform and its FFT analysis result, respectively. In Figure 8a, the grid-side current oscillates when the inverter starts. An FFT analysis is performed on the periodic waveform marked red in Figure 8a, with the results

shown in Figure 8b. The main disturbance components are the harmonics around 850 Hz, indicating that the 17th order resonance controller destroys the system stability. The THD of i_{L2} is 117.97%.

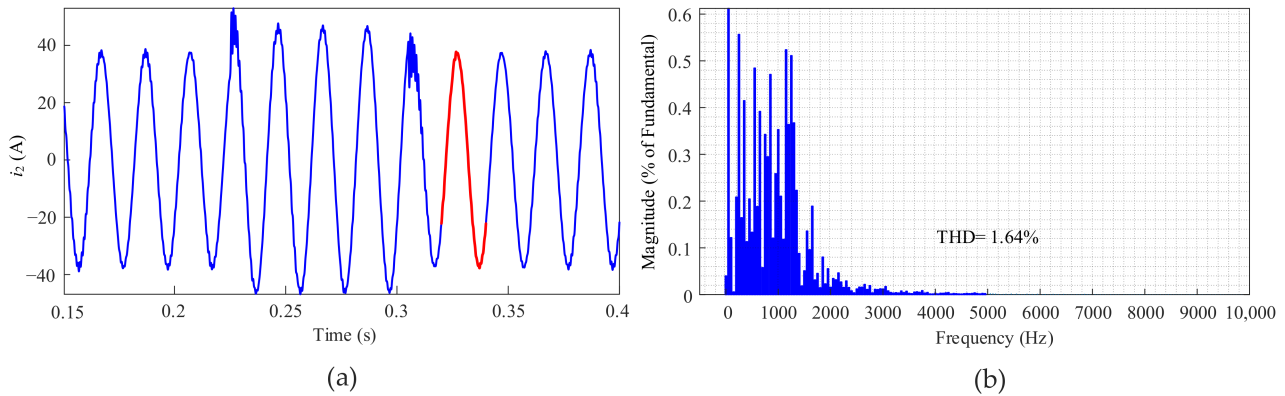


Figure 7. Simulation waveform of the grid-side current i_{L2} and its FFT analysis result in Simulation 1 when $L_g = 0$ and with the 5th, 7th, 11th, 13th order resonance controllers applied: (a) The simulation waveform; (b) the FFT analysis result.

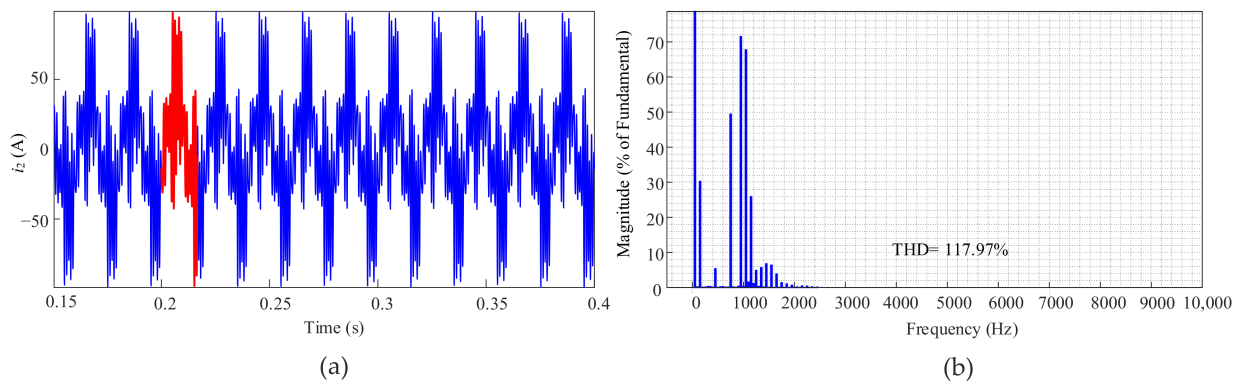


Figure 8. Simulation waveform of the grid-side current i_{L2} and its FFT analysis result in Simulation 2 when $L_g = 0$ and with the 5th order resonance controller applied: (a) The simulation waveform; (b) the FFT analysis result.

Simulation 3: Set $L_g = 2.6$ mH, the inverter-side reference current $i_{L1}^* = 30\sin\omega_0 t$ A. The voltage source contains the 5th order harmonic with an amplitude of 30 V. The 5th order resonance controller is used. Figure 9a,b show the grid-side current waveform and its FFT analysis result, respectively. In Figure 9a, the grid-side current is severely distorted. An FFT analysis is performed on the periodic waveform marked red in Figure 9a, with the results shown in Figure 9b. The main disturbance components are the harmonics at and around 250 Hz, indicating that the 5th resonance controller not only fails to suppress the 5th harmonic but also causes harmonic amplification, making the system unstable. The THD of i_{L2} is 107.14%.

The above analysis and simulation results indicate that the improved single-loop feedback control of the inverter-side current [15,22] allows only a few low-order resonant controllers to be used, which provides limited improvement on the grid-side current quality.

2.2.6. The Equivalent Grid-Side Current Single-Loop Feedback Control

Figure 1b3 shows the equivalent grid-side current single-loop feedback control, for which the stability region of the LCL resonant frequency is $(f_s/6, f_s/2)$ [4]. Compared with the inverter-side current single-loop feedback control in Figure 1b1,b2, a higher LCL resonant frequency can be set. Accordingly, more high-order harmonic resonance

controllers can be incorporated. However, when the grid inductance increases, the *LCL* resonant frequency may enter the instability region. The system instability can be avoided by setting the possible minimum *LCL* resonant frequency greater than $f_s/6$, but a large filter inductor is required to ensure the switching ripple attenuation performance [24].

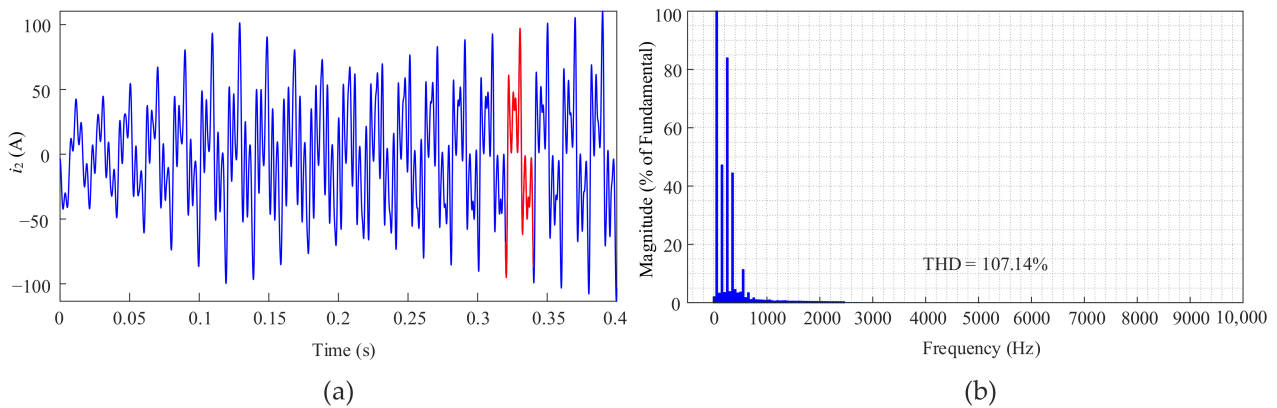


Figure 9. Simulation waveform of the grid-side current i_{L2} and its FFT analysis result in Simulation 3 when $L_g = 2.6$ mH and with the 5th order resonance controller applied: (a) The simulation waveform; (b) the FFT analysis result.

3. The Proposed Method for Passivity Enhancement

3.1. The Proposed Control Strategy

Figure 1b4 presents the control strategy proposed in this paper. A digital differentiator is applied to calculate the capacitor current. Next, the calculated capacitor current is subtracted from the detected inverter-side current, by which the equivalent grid-side current is obtained for feedback control. The calculated capacitor current and the detected capacitor voltage are used for active damping, which eliminates the *LCL* resonant frequency instability region. In this way, a higher *LCL* resonant frequency can be set compared with [15,22] without violating the system stability. More high-order harmonic resonant controllers can then be inserted, leading to a sinusoidal grid-side current. The PLC marked in Figure 1b4 is employed to enhance the system stability. Detailed analyses are presented in the following.

Figure 10 shows the block diagram of Figure 1b4. $G_i(s)$ is the current regulator. $G_{lead}(s)$ represents the PLC. $G_d(s)$ represents the time delay in the digital control, i.e., $G_d(s) = e^{-1.5T_s s}$, where T_s is the sampling period. K_{pwm} is the inverter bridge gain, i.e., $K_{pwm} = V_{in}/V_{tri}$, where V_{in} is the inverter DC-link voltage, and V_{tri} is the triangular carrier amplitude. H_{i1} and K are the proportional coefficients for active damping. H_{i2} is the sensor gain of the grid-side current i_{L2} . L_1 , C_f and L_2 compose the *LCL* filter. v_{PCC} represents the voltage at the point of common coupling (PCC). The parameters of the primary circuit and the controller are listed in Table 1. For comparison purposes, some parameters are the same as those in [24].

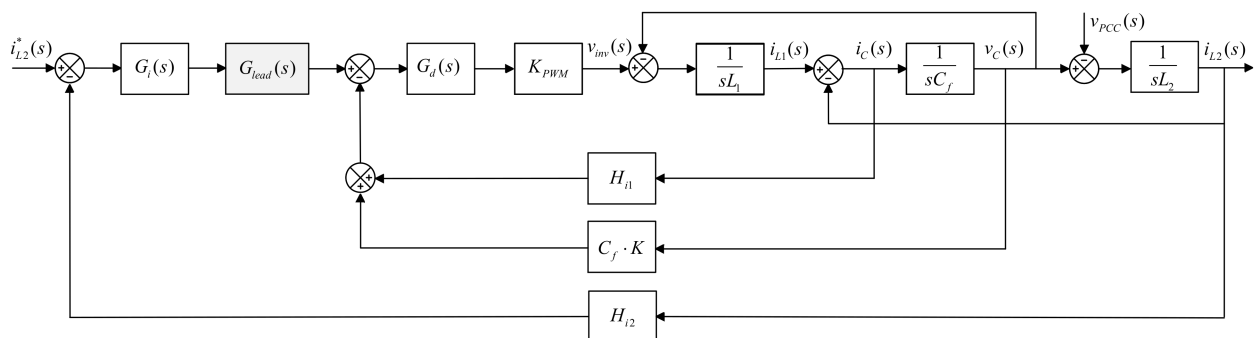


Figure 10. Block diagram of the proposed method in continuous-time domain.

3.2. Modeling of the Inverter Output Admittance

Figure 11a shows the simplified form of Figure 10, which is obtained through a series of equivalent transformations, where

$$G_{x1}(s) = \frac{G_i(s)G_d(s)K_{PWM}}{s^2L_1C_f + sC_f(H_{i1} + \frac{K}{s})G_d(s)K_{PWM} + 1} \quad (15)$$

$$G_{x2}(s) = \frac{s^2L_1C_f + sC_f(H_{i1} + \frac{K}{s})G_d(s)K_{PWM} + 1}{s^3L_1L_2C_f + s^2L_2C_f(H_{i1} + \frac{K}{s})G_d(s)K_{PWM} + s(L_1 + L_2)}. \quad (16)$$

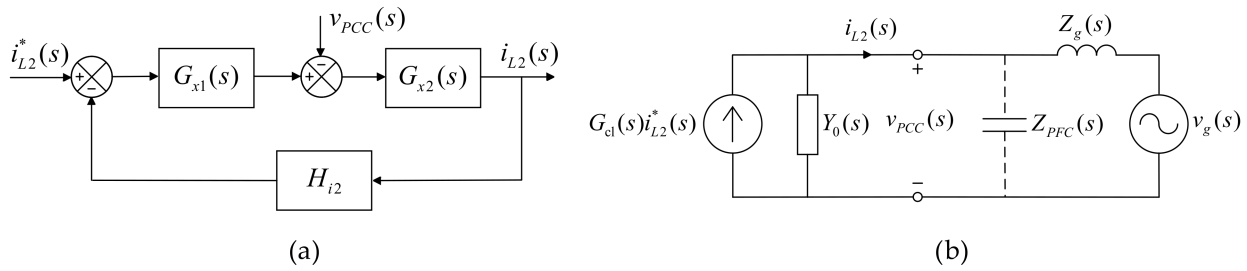


Figure 11. Simplified block diagram and the derived equivalent circuit [19]: (a) Equivalent form of Figure 10; (b) Norton equivalent circuit of a grid-connected inverter.

The open-loop transfer function is derived from Figure 11a as

$$T(s) = G_{x1}(s)G_{x2}(s)H_{i2} = \frac{H_{i2}G_i(s)G_d(s)K_{PWM}}{s^3L_1L_2C_f + s^2L_2C_f(H_{i1} + \frac{K}{s})K_{PWM}G_d(s) + s(L_1 + L_2)}. \quad (17)$$

To perform the passive analysis of the inverter output admittance, the grid-connected inverter is represented by the Norton equivalent circuit [19], as shown in Figure 11b. The grid-side current is derived as

$$i_{L2}(s) = G_{cl}(s)i_{L2}^*(s) - v_{PCC}(s) \cdot Y_o(s) \quad (18)$$

where $i_{L2}^*(s)$ is the grid-side reference current, $G_{cl}(s)$ is the closed-loop transfer function, $Y_o(s)$ is the inverter output admittance. $G_{cl}(s)$ and $Y_o(s)$ are denoted as

$$G_{cl}(s) = \frac{T(s)}{1 + T(s)}, \quad (19)$$

$$Y_o(s) = \frac{G_{x2}(s)}{1 + T(s)}. \quad (20)$$

3.3. Passive Analysis of the Inverter Output Admittance

Recalling the passivity theory [27], the inverter output admittance Y_o is passive if it satisfies (21), where ω_s is the sampling angular frequency.

$$\text{Re}\{Y_o(j\omega)\} \geq 0, \quad 0 \leq \omega \leq \omega_s/2 \quad (21)$$

Substituting $s = j\omega$ into (20) and taking its real part results in

$$\text{Re}\{Y_o(j\omega)\} = N \cdot (H_{i2}K_pK_c + (H_{i2}K_p - H_{i2}K_pL_1C_f\omega^2 + H_{i1}L_1C_f\omega^2) \cdot K_{PWM} \cos(1.5\omega T_s) - KL_1C_f\omega K_{PWM} \sin(1.5\omega T_s)). \quad (22)$$

In (22), N is positive for $0 \leq \omega \leq \omega_s/2$. Therefore, it is irrelevant to the passivity of Y_o . The expression is not listed due to its complexity. Figure 12 shows the frequency characteristic curve of $\text{Re}\{Y_o(j\omega)\}$.

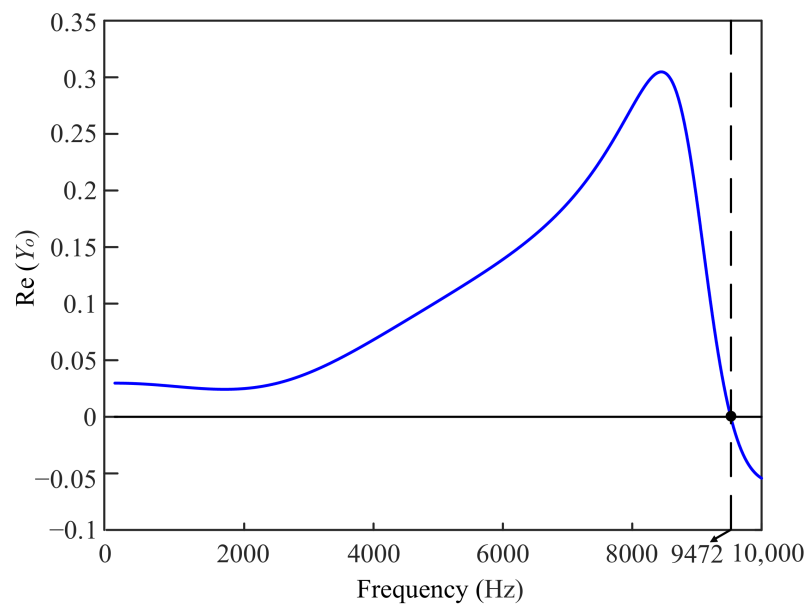


Figure 12. Frequency characteristic curve of $\text{Re}\{Y_o(j\omega)\}$.

In Figure 12, $\text{Re}\{Y_o(j\omega)\}$ is negative above 9472 Hz, indicating that the frequency range from 9472 Hz to 10,000 Hz (the Nyquist frequency $f_s/2$) is the non-passive region of $Y_o(j\omega)$.

3.4. The Proposed Passivity Enhancement Method

To eliminate the non-passive region, i.e., (9472 Hz, 10,000 Hz), this paper proposes to use a PLC [26] that corrects the phase of Y_o in this region to within $\pm 90^\circ$.

The transfer function of the PLC is given as

$$G_{lead}(s) = \frac{1 + \alpha_{lead}\tau_{lead}s}{1 + \tau_{lead}s} \quad (23)$$

where α_{lead} and τ_{lead} are the parameters, written as

$$\alpha_{lead} = \frac{1 + \sin \varphi_{m_lead}}{1 - \sin \varphi_{m_lead}} \quad (24)$$

$$\tau_{lead} = \frac{1}{\sqrt{\alpha_{lead}} \cdot \omega_{lead}} \quad (25)$$

where φ_{m_lead} is the phase lead provided at ω_{lead} . The maximum phase lag to compensate is about 6.9° , located at the Nyquist frequency. Accordingly, set $\varphi_{m_lead} = 30^\circ$ and $\omega_{lead} = \omega_s/2$ initially. $\alpha_{lead} = 1.42$ and $\tau_{lead} = 4 \times 10^{-5}$ can be calculated from (24) and (25), respectively, listed in Table 1. Figure 13 shows the phase diagrams of the output admittance Y_o (Y_o') before and after using the PLC.

Before using the PLC, the phase angle of Y_o satisfies $\angle Y_o(f) < -90^\circ, \forall f > 9472$ Hz. With the PLC applied, the output admittance is renamed Y_o' . The phase angle of Y_o' satisfies $\angle Y_o'(f) \in (-90^\circ, 90^\circ)$, i.e., $\text{Re}(Y_o'(f)) > 0, \forall f \in (0, f_s/2)$, which means the passivity is guaranteed for any Y_o' within $f \in (0, f_s/2)$. To summarize the proposed method, a flowchart is depicted in Figure 14.

3.5. Impact of the PLC on Other Critical Characteristics

This section explores what will happen to the performance of the original system when the PLC is added. When $L_g = 0$, it is verified that the original system has no open-loop right-half-plane pole [24]. The PLC has no open-loop right-half-plane pole either. Thus, no open-loop right-half-plane pole exists in the upgraded system. For the grid-side current

feedback control with active damping [24], Figure 15 shows the open-loop Bode plots before and after using the PLC under $L_g = 0$.

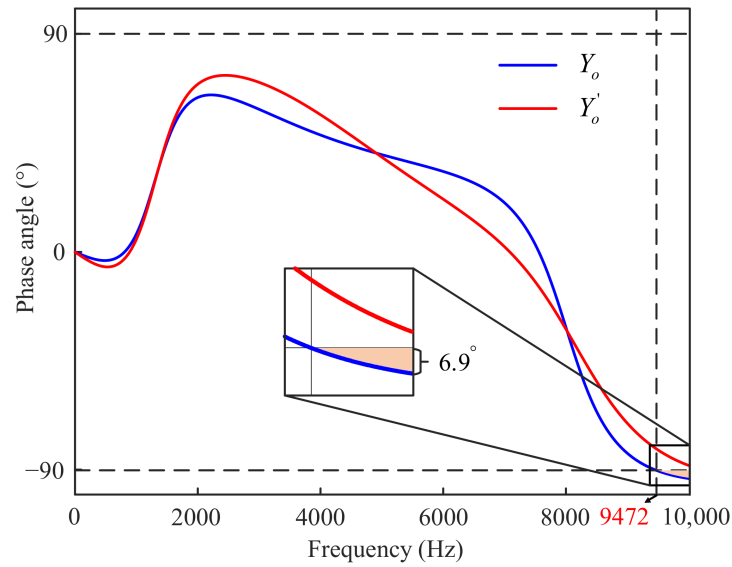


Figure 13. Phase diagrams of the output admittance before and after using the PLC.

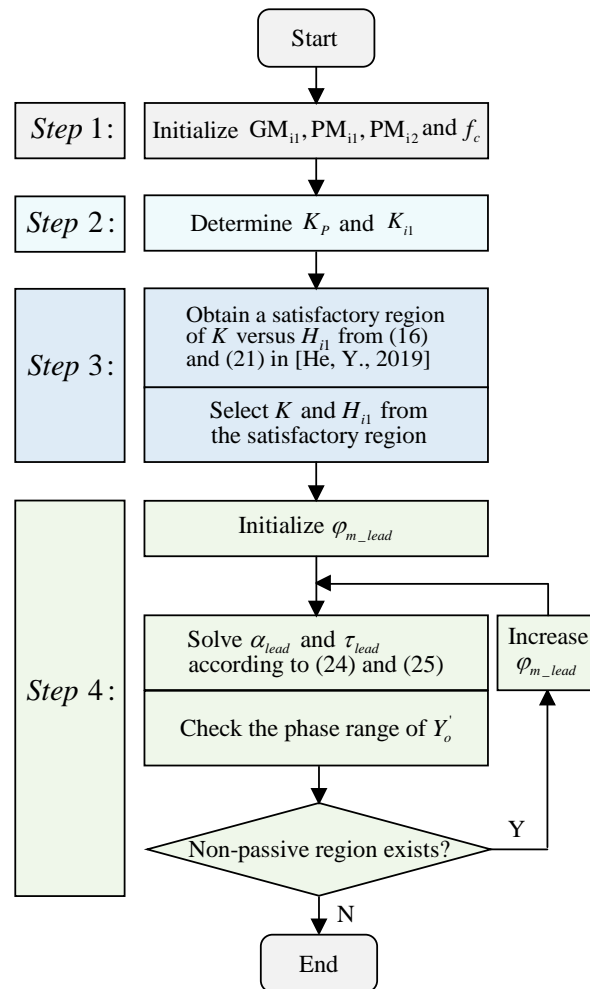


Figure 14. Flowchart of the proposed passivity enhancement method.

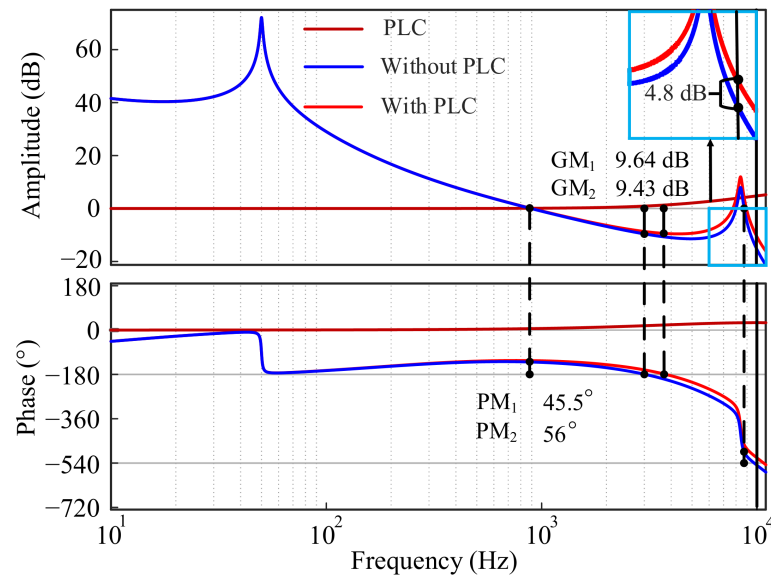


Figure 15. Bode plots of the PLC and the open-loop transfer functions before and after using the PLC [24].

In Figure 15, within the open-loop bandwidth, the characteristic curves of the original system and the upgraded system coincide essentially, while in the high-frequency range, both the amplitude–frequency and phase–frequency characteristic curves are raised by the PLC. At the Nyquist frequency, the amplitude increases the most, which is 4.8 dB. In fact, the slope beyond the *LCL* resonance frequency is close to -60 dB/dec, indicating that the high-frequency harmonic attenuation ability is slightly degraded but still meets the requirements. The phase margin PM_2 is 56° , an increase of 10° from PM_1 of the original system. The gain margin GM_2 is 9.43 dB, a decrease of 0.21 dB from GM_1 of the original system. PM_2 and GM_2 satisfy the stability margin requirements of no less than 45° and 3 dB [24], respectively, indicating that internal stability is preserved. Furthermore, a larger φ_{m_lead} results in a more sufficient phase margin for Y_o' , but will further reduce the attenuation of the high-frequency harmonics. For this reason, this paper selects $\varphi_{m_lead} = 30^\circ$ to achieve a balance between the stability and the harmonic attenuation.

The *s*-domain transfer functions from the inverter output voltage $v_{inv}(s)$ to the grid-side current $i_{L2}(s)$, to the capacitor current $i_c(s)$ and to the capacitor voltage $v_c(s)$ can be derived from Figure 10 as follows:

$$G_{iL2}(s) = \frac{i_{L2}(s)}{v_{inv}(s)} = \frac{1}{sL_1} \frac{\omega_{LTC}^2}{s^2 + \omega_{res}^2}, \quad (26)$$

$$G_{ic}(s) = \frac{i_c(s)}{v_{inv}(s)} = \frac{1}{sL_1} \frac{s^2}{s^2 + \omega_{res}^2}, \quad (27)$$

$$G_{vc}(s) = \frac{v_c(s)}{v_{inv}(s)} = \frac{1}{L_1 C_f} \frac{1}{s^2 + \omega_{res}^2}, \quad (28)$$

where $\omega_{LTC} = \sqrt{\frac{1}{L_T \cdot C_f}}$, $\omega_{res} = \sqrt{\frac{L_1 + L_T}{L_1 \cdot L_T \cdot C_f}}$, $L_T = L_2 + L_g$.

Discretizing (26)–(28) using the zero-order holder method yields

$$G_{iL2}(z) = \frac{i_{L2}(z)}{v_{inv}(z)} = \frac{T_s}{(L_1 + L_T)(z - 1)} - \frac{\sin(\omega_{res} T_s)}{\omega_{res} (L_1 + L_T)} \frac{z - 1}{z^2 - 2 \cos(\omega_{res} T_s) z + 1}, \quad (29)$$

$$G_{ic}(z) = \frac{i_c(z)}{v_{inv}(z)} = \frac{\sin(\omega_{res} T_s)}{\omega_{res} L_1} \frac{z - 1}{z^2 - 2 \cos(\omega_{res} T_s) z + 1}, \quad (30)$$

$$G_{vc}(z) = \frac{v_c(z)}{v_{inv}(z)} = \frac{L_T}{L_1 + L_T} \frac{(1 - \cos(\omega_{res}T_s))z + 1 - \cos(\omega_{res}T_s)}{z^2 - 2 \cos(\omega_{res}T_s)z + 1}, \quad (31)$$

The current regulator (1) is discretized with reference to [23]. A forward Euler integrator-based discretization method is used. The denominator with the sixth-order Taylor series is for enhancing the resonant pole accuracy. We obtain

$$G_i(z) = K_p + \sum_{h=1}^M K_{ih} T_s \frac{\cos(\theta_h) - z^{-1} \cos(\theta_h - \omega_h T_s)}{1 - 2z^{-1} \cos(\omega_h T_s) + z^{-2}}. \quad (32)$$

Discretizing the PLC (23) using the bilinear transform with prewarping at $f_s/2$, we obtain

$$G_{lead}(z) = \frac{a_1 z + a_2}{b_1 z + b_2} \quad (33)$$

where $a_1 = 1.257$, $a_2 = -0.4782$, $b_1 = 1$, $b_2 = -0.2215$.

Figure 16 shows the discrete time-domain control model corresponding to Figure 10. The grid voltage as an interference term does not affect the analysis results of this section, so it is ignored. To simplify the analysis process, the harmonic resonance controller in (32) is also neglected.

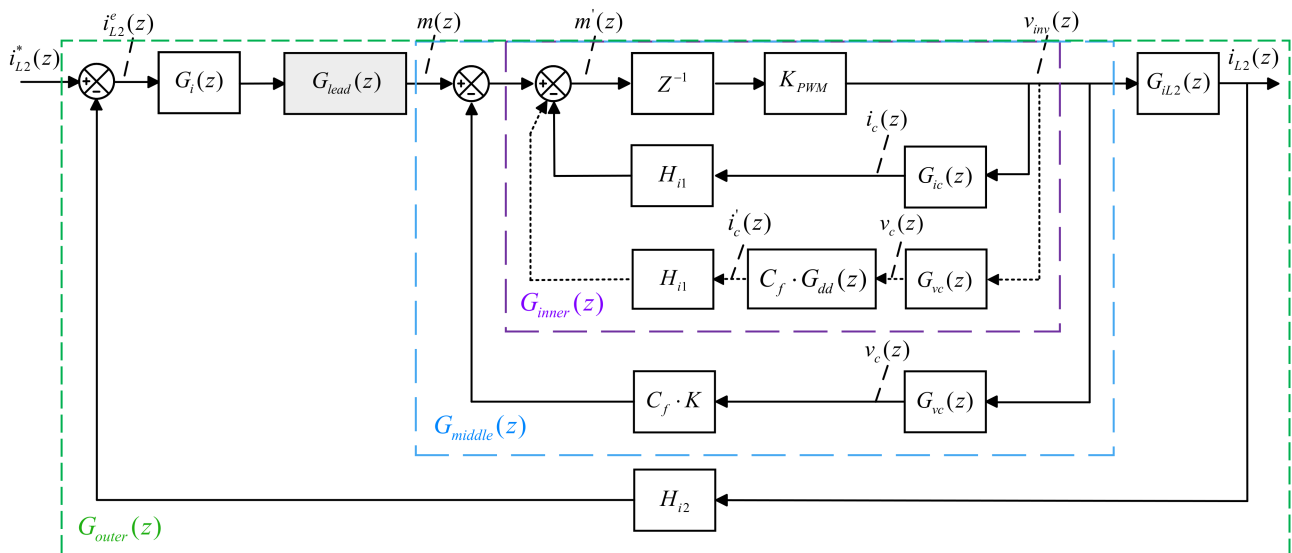


Figure 16. Block diagrams of the proposed control method in discrete-time domain.

In Figure 16, the control model comprises three feedback loops. The corresponding open-loop transfer functions are denoted as $G_{inner}(z)$, $G_{middle}(z)$ and $G_{outer}(z)$, with the expressions as

$$G_{inner}(z) = \frac{z^{-1} K_{PWM}}{1 + z^{-1} K_{PWM} H_{i1} G_{ic}(z)}, \quad (34)$$

$$G_{middle}(z) = \frac{G_{inner}(z)}{1 + G_{inner}(z) G_{vc}(z) C K}, \quad (35)$$

$$G_{outer}(z) = G_i(z) \cdot G_{lead}(z) \cdot G_{middle}(z) \cdot G_{iL2}(z) \cdot H_{i2}. \quad (36)$$

According to (36), Figure 17 plots the closed-loop pole diagram with the grid inductance variation, where the closed-loop pole diagram given in [24] is also plotted for comparison. The pair of closed-loop poles introduced by the resonant part of the current regulator is not given since they almost do not move. In Figure 17, even if the grid inductance varies widely, all the closed-loop poles are in the unit circle with a sufficient distance from it, demonstrating that the inverter still has good stability–robustness after applying the PLC.

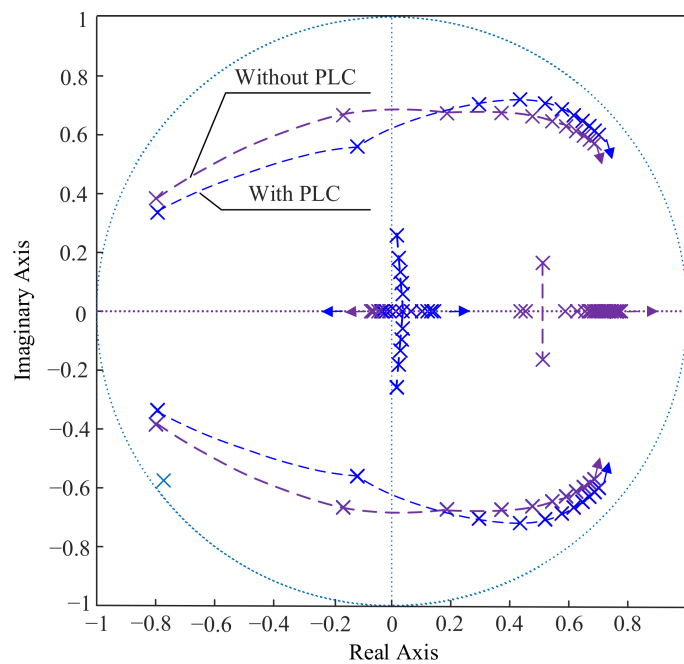


Figure 17. Closed-loop pole maps with the grid inductance variation [24].

3.6. Effect of the Calculated Capacitor Current on the Control Performance

In practical applications, the capacitance current can be calculated from the capacitance voltage utilizing a digital differentiator in (37), instead of installing a set of measurement devices, avoiding additional investment.

$$G_{dd}(z) = \frac{2}{T_s} \cdot \frac{z^2 + 0.5z - 0.5}{z^2 + 0.25z - 0.25} \cdot \frac{z - 1}{z + 1} \quad (37)$$

Figure 17 shows the Bode plots of the digital differentiator in (37) and the pure derivative for comparison. In [24], the grid inductance L_g may change from 0 to 2.6 mH. The corresponding LCL resonant frequency will vary over a wide range, i.e., [2788 Hz, 7885 Hz], as marked in Figure 18.

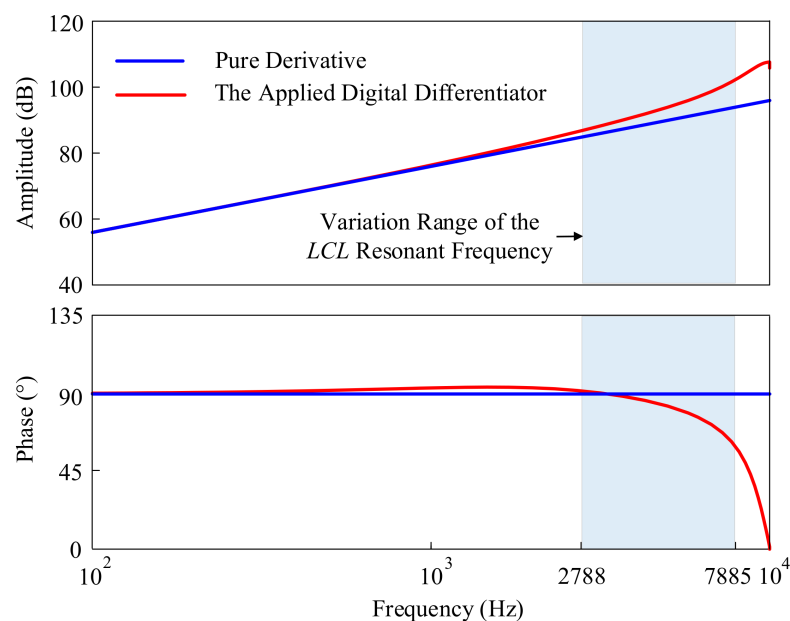


Figure 18. Bode plots of the digital differentiator and the pure derivative.

From Figure 18, the digital differentiator $G_{dd}(z)$ closely matches the pure derivative in a wide frequency range. Furthermore, in the low-frequency range, the reactance of C_f is much larger than that of L_1 and L_2 , resulting in a negligible capacitance current, so the calculation error of the capacitance current is negligible. Therefore, for this frequency range, the difference between the measured inverter-side current and the calculated capacitor current can be used to achieve the equivalent grid-side current feedback control [36]. In contrast, in the high-frequency range, the phase-frequency curve drops rapidly, which may cause the digital differentiator to lose its derivative characteristic so that the calculated capacitance current will lose its usefulness in active damping.

$i_c(z)$ is replaced with the calculated capacitor current $i_c'(z)$ for feedback, whose feedback path is depicted by a dashed line in Figure 16. Figure 19 shows the corresponding closed-loop pole map according to (35), where $G_{ic}(z)$ in (33) is substituted by $C_f \bullet G_{dd}(z) \bullet G_{vc}(z)$. In Figure 19, a pair of closed-loop conjugate poles is outside the unit circle when $L_g = 0$, indicating an unstable system. As L_g increases, the closed-loop conjugate poles gradually move into the unit circle, which means the system becomes stable. From Figures 18 and 19, the system stability is influenced by the damping effect of i_c' , determined by the proximity of i_c' to i_c . For the LCL filter parameters in Table 1, the corresponding LCL resonant frequency is above the highest frequency that i_c' can provide effective damping. Consequently, to use the calculated capacitor current for active damping, these LCL filter parameters need to be modified. A higher LCL resonant frequency requires smaller LCL elements, for which above $f_s/6$ is cost-effective. However, the ripple attenuation capacity decreases as the LCL resonant frequency increases. For this reason, a compromise should be made when designing an LCL filter. A further study on this is out of the scope of this paper.

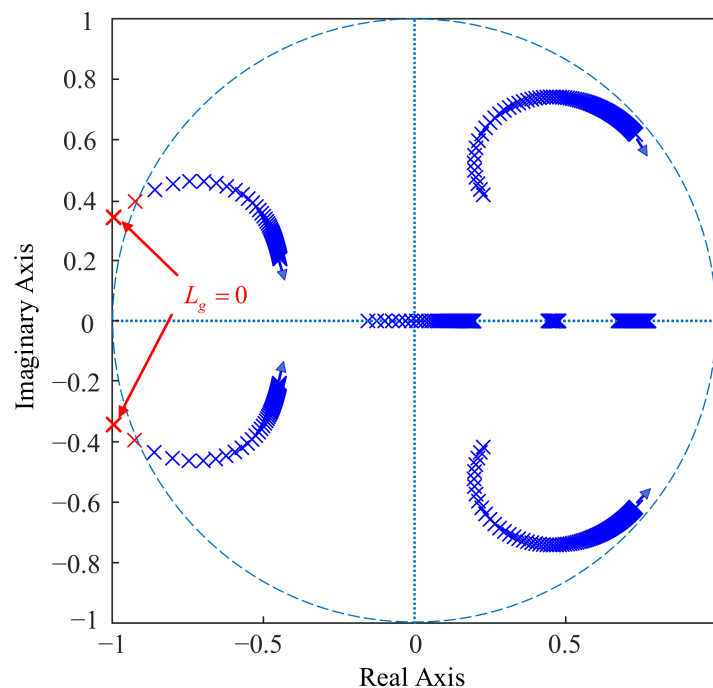


Figure 19. Closed-loop pole map using the calculated capacitor current i_c' for control.

4. A Case Study on Stability Evaluation

4.1. System Description

Figure 20 displays a typical per-phase topology diagram of multiple renewable energy inverters connected to the grid through a power cable. The power cable is represented by the Π -type equivalent circuit, assuming that each section has the same parameters. C_1 represents the capacitive load connected to point A, L_g represents the grid inductance and C_{CPF} represents the power factor correction capacitor. View from the PCC point, when C_{CPF} is installed, the grid is inductive or capacitive, and when it is not installed, the grid is

inductive. For both cases, the grid impedance is generally passive. The above parameters are listed in Table 1.

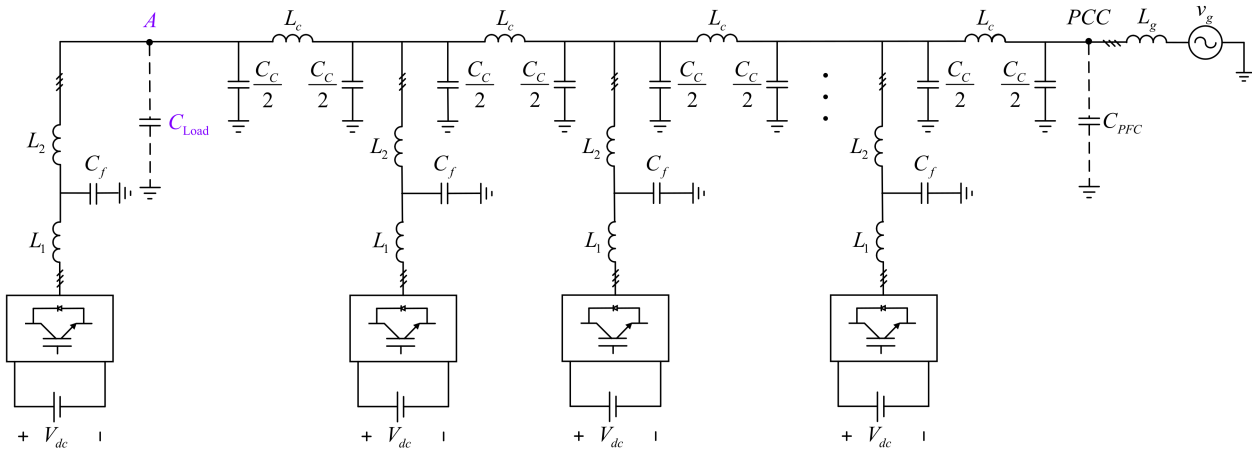


Figure 20. Per-phase diagram of multiple inverters connected to the grid [28].

Figure 21 depicts the admittance-based equivalent circuit of Figure 20. Four inverters are considered in this case. The inverter at point A is taken as the analysis object, which is represented by the Norton equivalent circuit. The other inverters are represented by the output admittance Y_o . For the inverter connected to point A, the equivalent load admittance Y_{Load} is the series-parallel combination of the grid admittance, the admittance of each section of the power cable, the output admittance of other inverters, and the admittance of the capacitive load connected to point A.

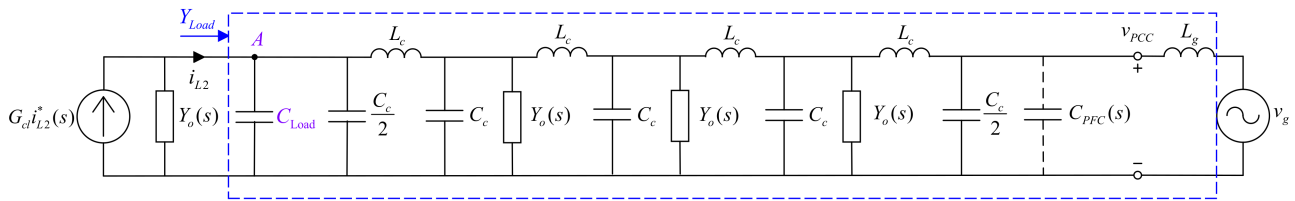


Figure 21. Admittance-based equivalent circuit of Figure 20 [28].

4.2. Stability Evaluation of the Proposed Method

Considering the equivalent load admittance Y_{Load}' 's effect, the closed-loop response is expressed as

$$i_{L2}(s) = \frac{1}{1 + Y_o(s)/Y_{Load}'(s)} \cdot G_{cl}(s) \cdot i_{L2}^*(s). \tag{38}$$

Internal stability can be satisfied if the closed-loop transfer function $G_{cl}(s)$ is stable. For an inverter with internal stability, its external stability depends on the minimum feedback loop formed by $Y_o(s)$ and $Y_{Load}'(s)$ [28]. Figure 22 shows the frequency response of the inverter output admittance Y_o (Y_o') and the equivalent load admittance Y_{Load} (Y_{Load}') before and after using the PLC.

In Figure 22a, before using the phase lead compensator, the intersection point of the amplitude–frequency response of Y_{Load} and Y_o is located in the non-passive region of Y_o . At the intersection frequency, the phase angle difference between Y_{Load} and Y_o is above 180° , which means the phase margin of the minimum feedback loop is negative, indicating that an LC resonance may be triggered. With the PLC, Y_o' is passive all over the controllable frequency range, i.e., $(0, f_s/2)$. Since all components of Y_{Load}' are passive, Y_{Load}' is also passive [28]. As illustrated in Figure 22b, the phase angle difference between Y_o' and Y_{Load}' is less than 180° all over $(0, f_s/2)$, which means the phase margin of the minimum feedback loop is positive, indicating that the LC resonance risk has been eliminated. It can

be concluded from above that internal and external stability can be satisfied for inverters with the proposed control strategy.

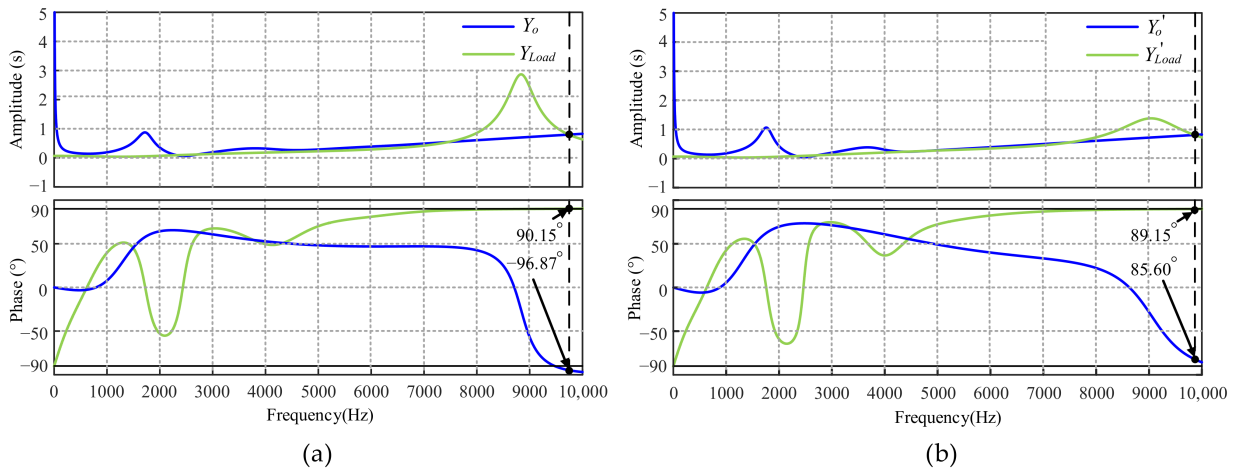


Figure 22. Frequency response of the inverter output admittance and the equivalent load admittance: (a) Before using the PLC; (b) after using the PLC.

5. Analysis of the Harmonic Suppression Capability of the Proposed Method

When the grid inductance $L_g = 0$, taking the LCL parameters from Table 1 into (2), the initial resonant frequency can be obtained as $f_{r0_pro} \approx 7885$ Hz. When L_g increases to 10% per unit, i.e., 2.6 mH [24], replacing L_2 in (2) with $L_T = L_2 + L_g$, the actual resonant frequency is obtained as $f_{r_pro} \approx 2788$ Hz. Both f_{r0_pro} and f_{r_pro} are much higher than f_{r0_inv} and f_{r_inv} in Section 2.2. Therefore, the LCL resonant frequency characteristics are less restrictive for the use of resonant controllers. The following will verify that more high-order resonant controllers can be inserted to improve the grid-side current quality.

According to the analysis in Section 2.2, to reduce the current distortion during inverter start-up or step change of the reference current, Figure 23 is substituted for Figure 10, where A denotes the harmonic resonance controllers, B denotes the proportional controller plus the fundamental resonance controller, as given in (3) and (4), respectively.

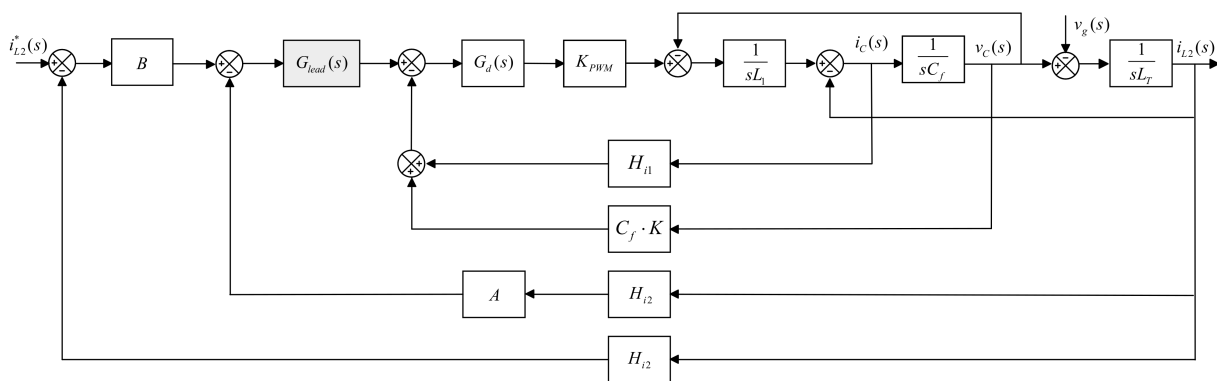


Figure 23. Block diagram of the proposed method transformed from Figure 10.

Performing a series of equivalent transformations on Figure 23 obtains the equivalent block diagrams given in Figure A1 of Appendix A, from which the following transfer functions can be derived.

The open-loop transfer function from i_{L2}^* to i_{L2} is expressed as

$$G_{ol_pro}(s) = \frac{G_{lead}(s)G_d(s)K_{PWM}H_{i2}B}{L_1L_TC_f s^3 + L_TC_f(sH_{i1} + K)K_{PWM}G_d(s)s + s(L_1 + L_T) + G_{lead}(s)G_d(s)K_{PWM}H_{i2}A} \tag{39}$$

The closed-loop transfer function from i_{L2}^* to i_{L2} is expressed as

$$G_{cl_pro}(s) = \frac{G_{lead}(s)G_d(s)K_{PWM}H_{i2}B}{L_1L_T C_f s^3 + L_T C_f G_d K_{PWM}(H_{i1}s + K)s + (L_1 + L_T)s + G_{lead}(s)G_d(s)K_{PWM}H_{i2}(A + B)}. \quad (40)$$

The closed-loop transfer function from v_g to i_{L2} is expressed as

$$G_{vcl_pro} = \frac{L_1 C_f s^2 + G_d(s)K_{PWM}C_f H_{i1}s + G_d(s)K_{PWM}C_f K + 1}{L_1 L_T C_f s^3 + G_d(s)K_{PWM}L_T C_f H_{i1}s^2 + (L_1 + L_T + G_d(s)K_{PWM}L_T C_f K)s + (A + B)H_{i2}G_{lead}(s)G_d(s)K_{PWM}}. \quad (41)$$

The Bode plot of $G_{ol_pro}(s)$ is shown in Figure 24a when $L_g = 0$. To make it easy to observe, the highest order of the harmonic resonance controller applied is the 67th order. The phase margin PM_1 is 47.5° . The gain margin GM_1 is 9.44 dB. They both satisfy the stability margin requirements of the classical control theory, i.e., $PM \in [30^\circ, 60^\circ]$, $GM \geq 3\text{--}6$ dB [10].

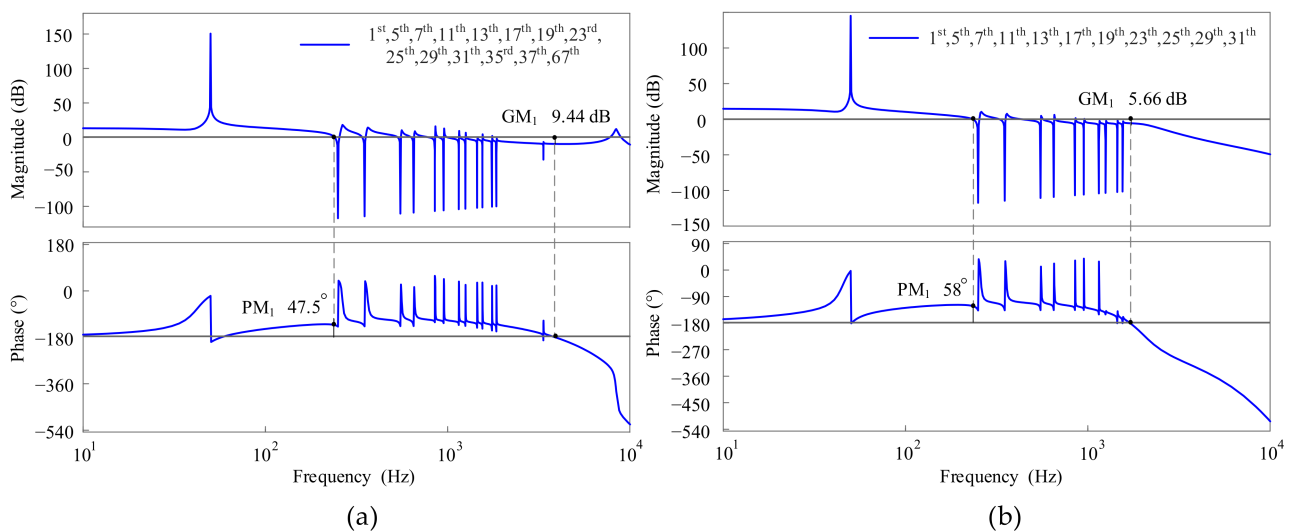


Figure 24. Bode plots of the open-loop transfer function $G_{ol_pro}(s)$: (a) $L_g = 0$; (b) $L_g = 2.6$ mH.

The Bode plot of $G_{ol_pro}(s)$ is shown in Figure 24b when $L_g = 2.6$ mH. For ease of observation, the highest order of the harmonic resonance controller applied is the 31st order. The phase margin PM_1 and the gain margin GM_1 of $G_{ol_pro}(s)$ are 58° and 5.66 dB, respectively. They both satisfy the stability margin requirements of the classical control theory.

It can be drawn from above that by suppressing the LCL resonance, the restriction of it on the stability of resonant controllers is mitigated. A higher LCL resonant frequency than that of [15] further extends the harmonic rejection range.

The Bode plots of $G_{cl_pro}(s)$ are shown in Figure 25a,b when $L_g = 0$ and $L_g = 2.6$ mH, respectively. Note that unlike the amplitude–frequency response of $G_{cl}'(s)$ in Figure 4a, $G_{cl_pro}(s)$ has no spike near the LCL resonant frequency, which will not cause the harmonic current amplification when a step change of the grid-side current reference value occurs.

The Bode plots of $G_{vcl_pro}(s)$ are shown in Figure 26a,b when $L_g = 0$ and $L_g = 2.6$ mH, respectively, which illustrates that the resonant frequency components of the grid-side current, including the fundamental component and harmonic components, can be effectively attenuated.

To sum up, as for the improved inverter-side current single-loop feedback control schemes [15,22] in Section 2.2, when $L_g = 0$, the highest order of the harmonic resonance controller available is the 13th order. When $L_g = 2.6$ mH, it is hard to use a resonance controller to suppress any characteristic harmonic. In this paper, the available order of the harmonic resonance controller is much higher than that of [15] and [24] in both cases, which means that the current quality at the grid side can be significantly improved.

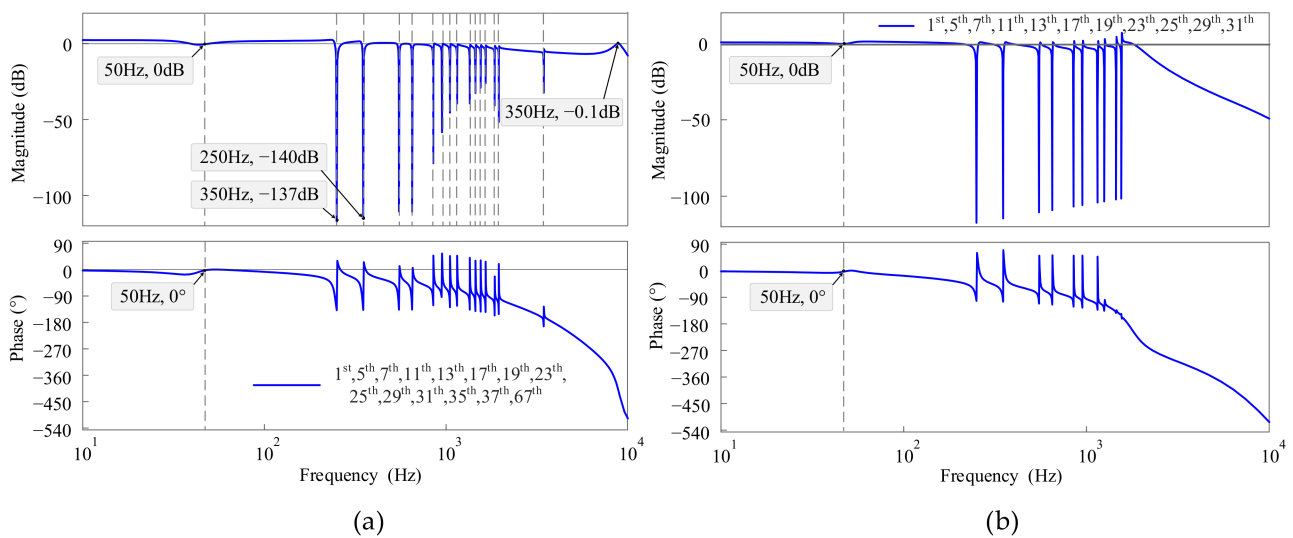


Figure 25. Bode plots of the closed-loop transfer function $G_{cl_pro}(s)$: (a) $L_g = 0$; (b) $L_g = 2.6$ mH.

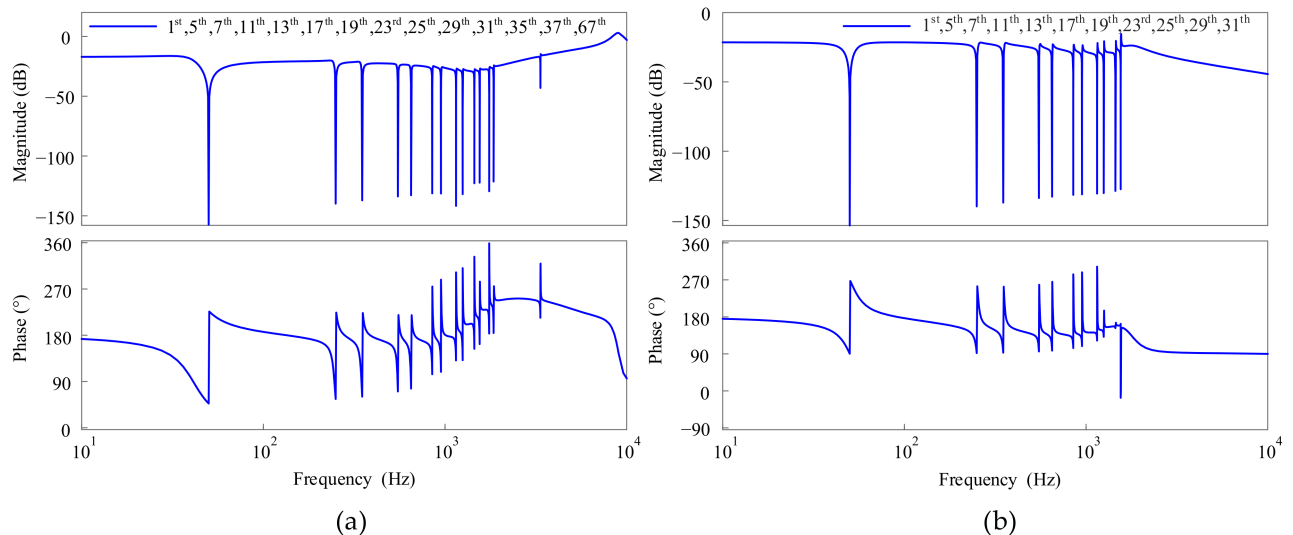


Figure 26. Bode plots of the closed-loop transfer function $G_{vcl_pro}(s)$: (a) $L_g = 0$; (b) $L_g = 2.6$ mH.

6. Simulation and Experimental Verification

For validating the analysis in the above sections, simulations and experiments are performed with the parameters listed in Table 1. The simulations are conducted on Matlab/Simulink. The experimental setup is shown in Figure 27. The modulation strategy is space vector modulation with a 10 kHz switching frequency for IGBT.

6.1. Case 1: Verification of the Analysis in Section 3.6

The active damping is performed with the capacitance current measurement value i_c before t_1 and the calculated value i_c' after t_1 . The simulated waveform of the grid-side current and the FFT analysis of the part marked red are shown in Figure 28a1,a2. The corresponding experimental waveform is shown in Figure 28a3. When i_c' is used instead of i_c for control, the LCL resonance damping fails, and the protection device shuts off the inverter from the grid, preventing the inverter from being damaged by overcurrent. The results confirm the correctness of the analysis results in Section 3.6.

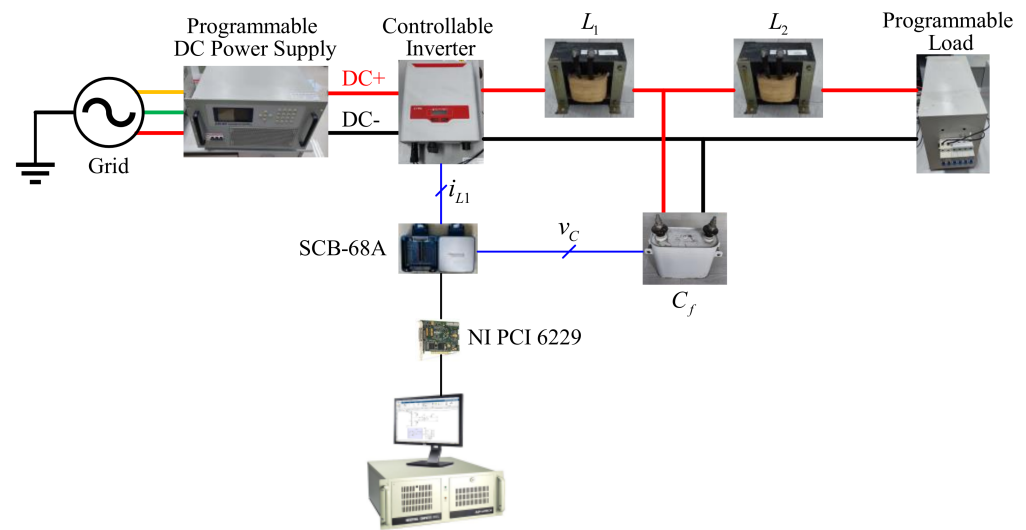


Figure 27. Configuration of the experimental setup.

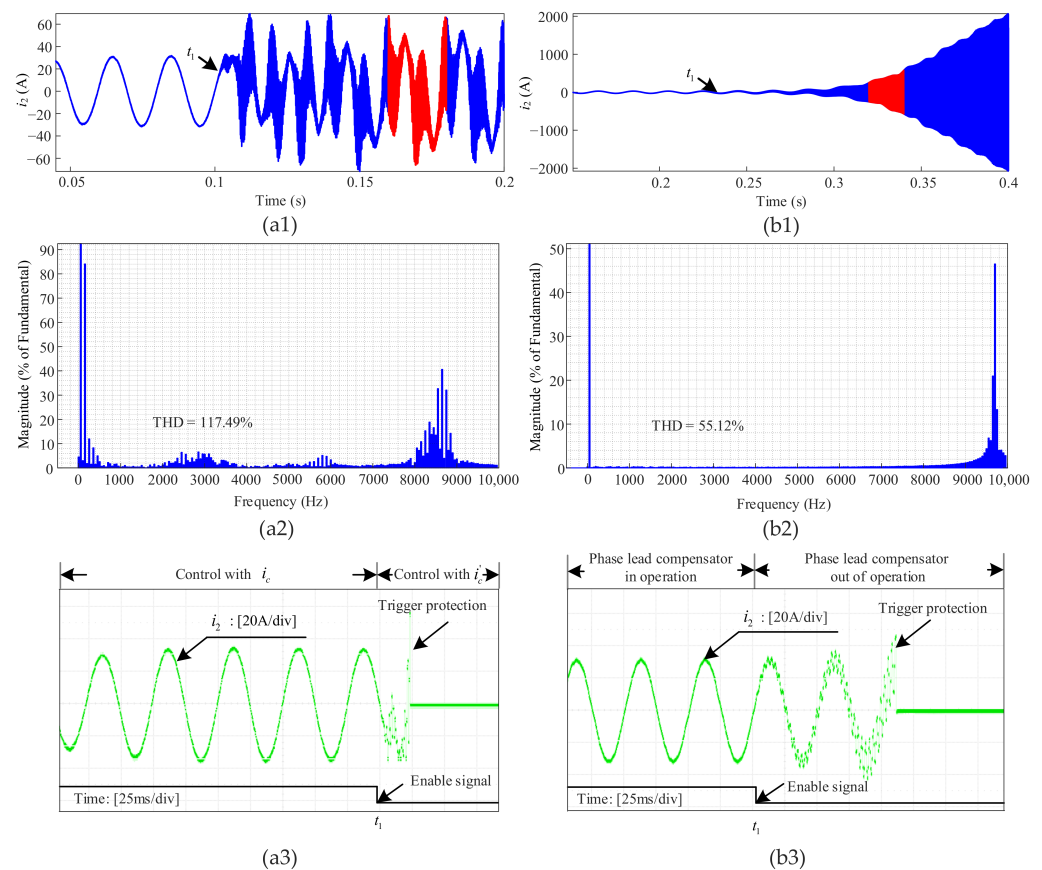


Figure 28. Simulation and experimental results of case 1 and case 2: (a1,a2) Simulation results of the grid-side current i_{L2} and its FFT analysis for case 1; (b1,b2) simulation results of the grid-side current i_{L2} and its FFT analysis for case 2; (a3,b3) experimental results of the grid-side current i_{L2} for case 1 and case 2, respectively.

6.2. Case 2: Verification of the Stability-Enhancing Effect of the Proposed Method

The PLC is applied before t_1 and exited at t_1 . The simulated waveform of the grid-side current and its FFT analysis result are shown in Figure 28b1,b2. The corresponding experimental waveform is shown in Figure 28b3. Figure 28b1 illustrates that the inverter operates stably with the proposed PLC. When the PLC is exited, the grid-side current

starts to oscillate and diverge, indicating the system is unstable [37]. Figure 28b2 shows the corresponding FFT analysis result. From Figure 28b2, the disturbance components are close to the crossover frequency in Figure 22a, which proves that the oscillation of the grid-side current is caused by the resonance between the inverter output admittance and the equivalent load admittance, validating the analysis in Section 4.2. Figure 28b3 shows that the resonated current trips the overcurrent protection after the enable signal is triggered. The results verify the stability-enhancing effect of the proposed method.

6.3. Case 3: Verification of the Harmonic Suppression Capability of the Proposed Method

The performance of the proposed control method is tested under severely distorted grid voltage. The grid-side reference current i_{L2}^* experiences a step change from 30 A to 40 A at t_1 and jumps back to 30 A after 0.08 s.

For $L_g = 0$, the grid voltage contains harmonic components of $6k \pm 1$ th with an amplitude of 30 V, $k = 1, 2, \dots, 11$. Correspondingly, the harmonic resonance controllers of $6k \pm 1$ th are applied, $k = 1, 2, \dots, 11$. In Figure 29a1, during the half cycle after i_{L2}^* jumps, the waveform of i_{L2} is not distorted. In Figure 29a2, the THD of i_{L2} is 3.35%, much lower than the 5% required by the grid standard [34]. The experimental result in Figure 29a3 is consistent with the simulation results.

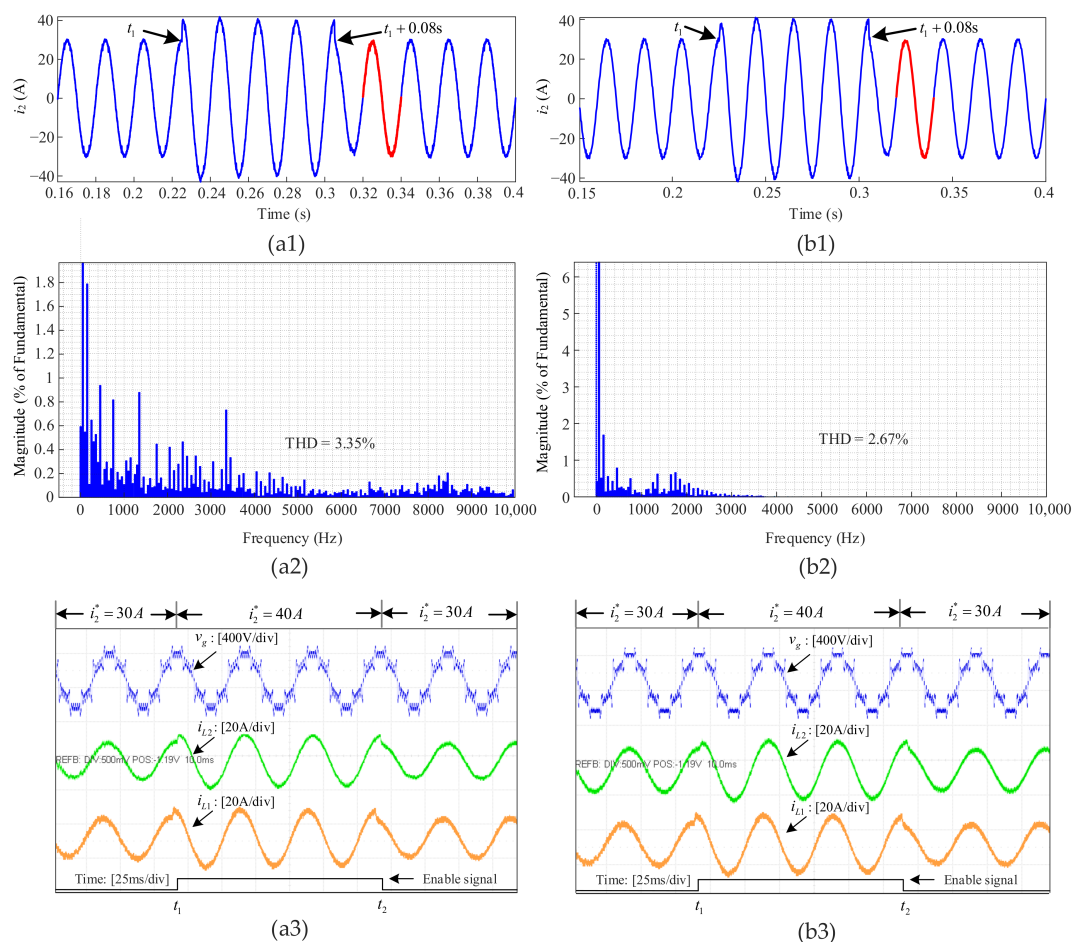


Figure 29. Simulation and experimental results of case 3: (a1,a2) Simulation results of the grid-side current i_{L2} and its FFT analysis for $L_g = 0$; (b1,b2) simulation results of the grid-side current i_{L2} and its FFT analysis for $L_g = 2.6$ mH; (a3,b3) experimental results of the grid-side current i_{L2} and the inverter-side current i_{L1} under the distorted grid voltage v_g for $L_g = 0$ and $L_g = 2.6$ mH, respectively.

For $L_g = 2.6$ mH, the grid voltage contains harmonic components of $6k \pm 1$ th with an amplitude of 30 V, $k = 1, 2, \dots, 6$. Correspondingly, the harmonic resonance controllers of

$6k \pm 1$ th are applied, $k = 1, 2, \dots, 6$. In Figure 29b1, during the half cycle after i_{L2}^* jumps, the waveform of i_{L2} is close to a sine wave. In Figure 29b2, the THD of i_{L2} is 2.67%, which is in compliance with the grid requirements. The experimental result in Figure 29b3 is consistent with the simulation results.

The results verify that the proposed control strategy achieves excellent grid-side current harmonic suppression.

7. Conclusions

The emphasis of this paper lies in enhancing the stability and harmonic suppression capability of *LCL*-type grid-connected inverters. The main contributions can be summarized as follows:

(1) The improved inverter-side current single-loop feedback control achieves controllability of the grid-side current harmonics, but the harmonic rejection range is narrow due to the stability requirement. The grid-side current feedback control with active damping permits higher-order resonance controllers to be used, further mitigating the grid-side current harmonic distortion.

(2) The PLC can elevate the phase of the inverter output admittance, making the real part of the inverter output admittance positive in the controllable frequency range, which means that the inverter output admittance is passive.

(3) When multiple inverters are connected to a non-ideal grid, making each inverter adopt the proposed control method, the potential resonance risk in the system can be eliminated.

(4) The calculated capacitor current can achieve the equivalent grid-side current feedback control and active damping, enabling the inverter to perform well without additional measuring devices.

Simulation and experimental results have confirmed the effectiveness of the proposed method.

Author Contributions: Conceptualization, X.W.; methodology, X.W.; software, X.W.; validation, S.Z.; formal analysis, X.W.; investigation, X.W.; resources, X.W.; data curation, X.W.; writing—original draft preparation, X.W.; writing—review and editing, X.W.; visualization, X.W.; supervision, D.W.; project administration, D.W.; funding acquisition, X.W. All authors have read and agreed to the published version of the manuscript.

Funding: This research received no external funding.

Institutional Review Board Statement: Not applicable.

Informed Consent Statement: Not applicable.

Data Availability Statement: Not applicable.

Conflicts of Interest: The authors declare no conflict of interest.

Abbreviations

The following abbreviations are used in this manuscript:

FFT	Fast Fourier transform
PMSG	Permanent magnet synchronous generator
LCL	Inductive–capacitive–inductive
PLC	Phase lead compensator
PWM	Pulse-width modulation
THD	Total harmonic distortion
PLL	Phase-locked loop
PR	Proportional resonant controller
PCC	Point of common coupling
GM	Gain margin
PM	Phase margin

Nomenclature

Parameters

L_1	Inverter-side inductance (μH)
L_2	Grid-side inductance (μH)
C_f	Filter capacitance (μF)
L_g	Equivalent grid inductance (μH)
L_T	The sum of L_2 and L_g (μH)
L_c	Feeder inductance (μH)
C_c	Feeder capacitance (μF)
C_{load}	Load equivalent capacitance (μF)
T_s	Sampling period (s)
f_s	Sampling frequency (kHz)
f_0	Grid fundamental frequency (Hz)
f_{r0_inv}	The initial resonant frequency of the <i>LCL</i> filter set in Section 2 (Hz)
f_{r_inv}	The actual resonant frequency of the <i>LCL</i> filter set in Section 2 (Hz)
f_{r0_pro}	The initial resonant frequency of the <i>LCL</i> filter set in Sections 3–6 (Hz)
f_{r_pro}	The actual resonant frequency of the <i>LCL</i> filter set in Sections 3–6 (Hz)
ω_s	Sampling angular frequency (rad/s)
ω_{res}	The <i>LCL</i> resonance angular frequency (rad/s)
ω_{LTC}	The anti-resonance angular frequency (rad/s)
Y_o	The inverter output admittance before using the phase lead compensator (S)
Y_{Load}	The series-parallel combination of the grid admittance before using the phase lead compensator (S)
Y_o'	The inverter output admittance after using the phase lead compensator (S)
Y_{Load}'	The series-parallel combination of the grid admittance after using the phase lead compensator (S)

Sets

α_{lead}	Lead compensator factor
τ_{lead}	Lead compensator factor
φ_{m_lead}	The desired leading phase provided by the lead compensator ($^\circ$)
ω_{lead}	The angular frequency at which φ_{m_lead} is arranged (rad/s)

Variables

i_{L1}^*	The inverter-side reference current (A)
i_{L2}^*	The grid-side reference current (A)
i_{L1}	The inverter-side current (A)
i_{L2}	The grid-side current (A)
i_c	The <i>LCL</i> capacitor current (A)
i_c'	The calculated <i>LCL</i> capacitor current (A)
v_c	The <i>LCL</i> capacitor voltage (V)
v_g	The grid voltage (V)
V_{inv}	The inverter output voltage (V)
V_{in}	Amplitude of the DC-link voltage (V)
V_{tr}	Amplitude of the triangular carrier (V)
H_i	Sensor gain of the grid-side current and the inverter-side current (denoted in Section 2)
H_{i1}	Capacitor current feedback coefficient for active damping
K	Capacitor voltage feedback coefficient for active damping
H_{i2}	Sensor gain of the grid-side current (denoted in Sections 3–5)
ω_0	Fundamental angular frequency (rad/s)
ω_h	The angular frequency at $h\omega_0$ (rad/s)
K_p	Proportional gain of the PR controller
K_{ih}	Resonant gain of the PR controller at ω_h
θ_h	The desired leading angle ($^\circ$)
K_{pwm}	The inverter bridge gain

Appendix A

In this appendix, a series of equivalent block diagrams transformed from Figure 22 are illustrated in Figure A1. To obtain the transfer function from the grid voltage v_g to the grid-side current i_{L2} , the grid-side current reference i_{L2}^* is set to 0 in Figure A1d–f. From Figure A1, the transfer functions (39)–(41) can be obtained, as given in Section 5.

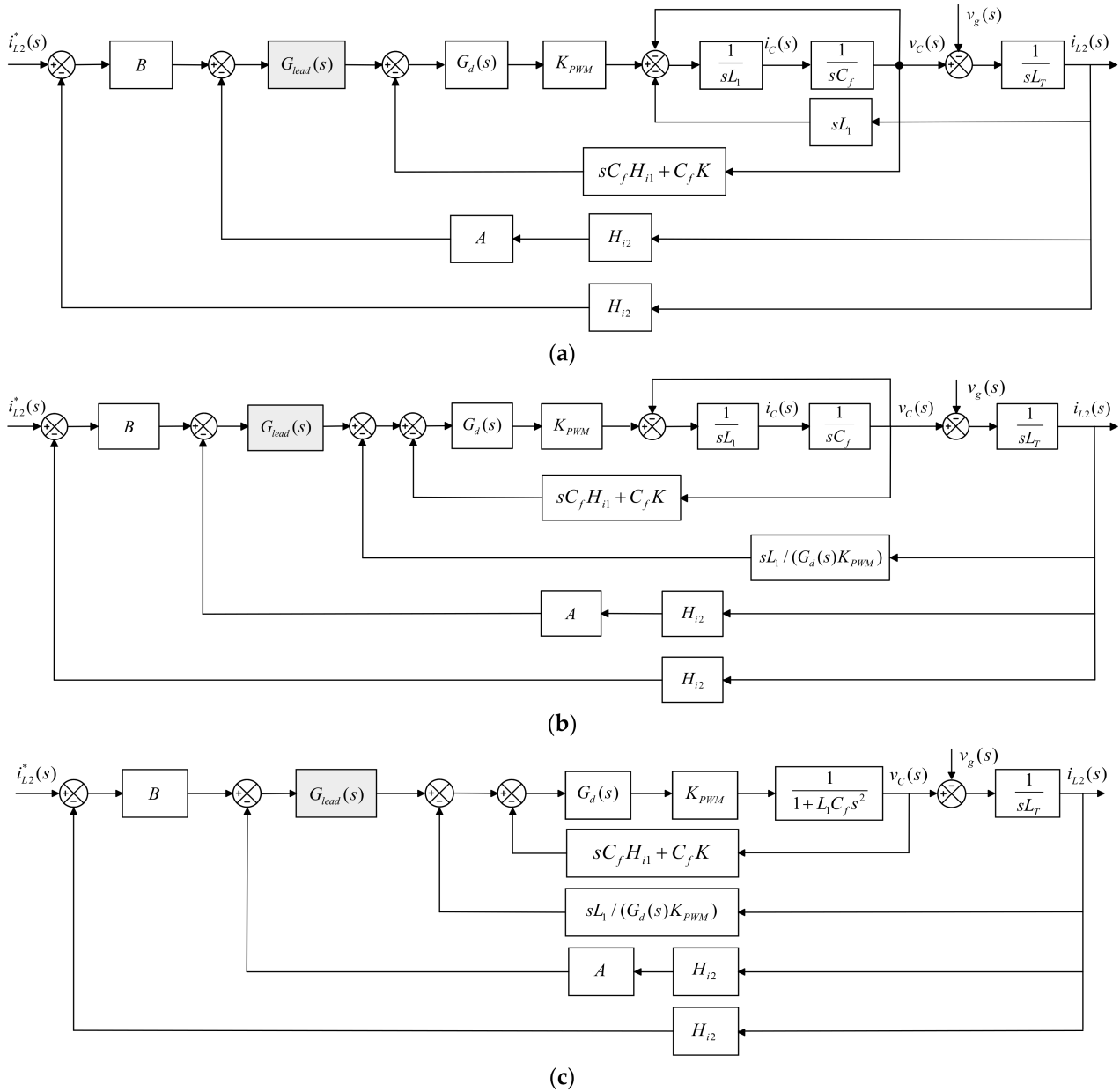


Figure A1. Cont.

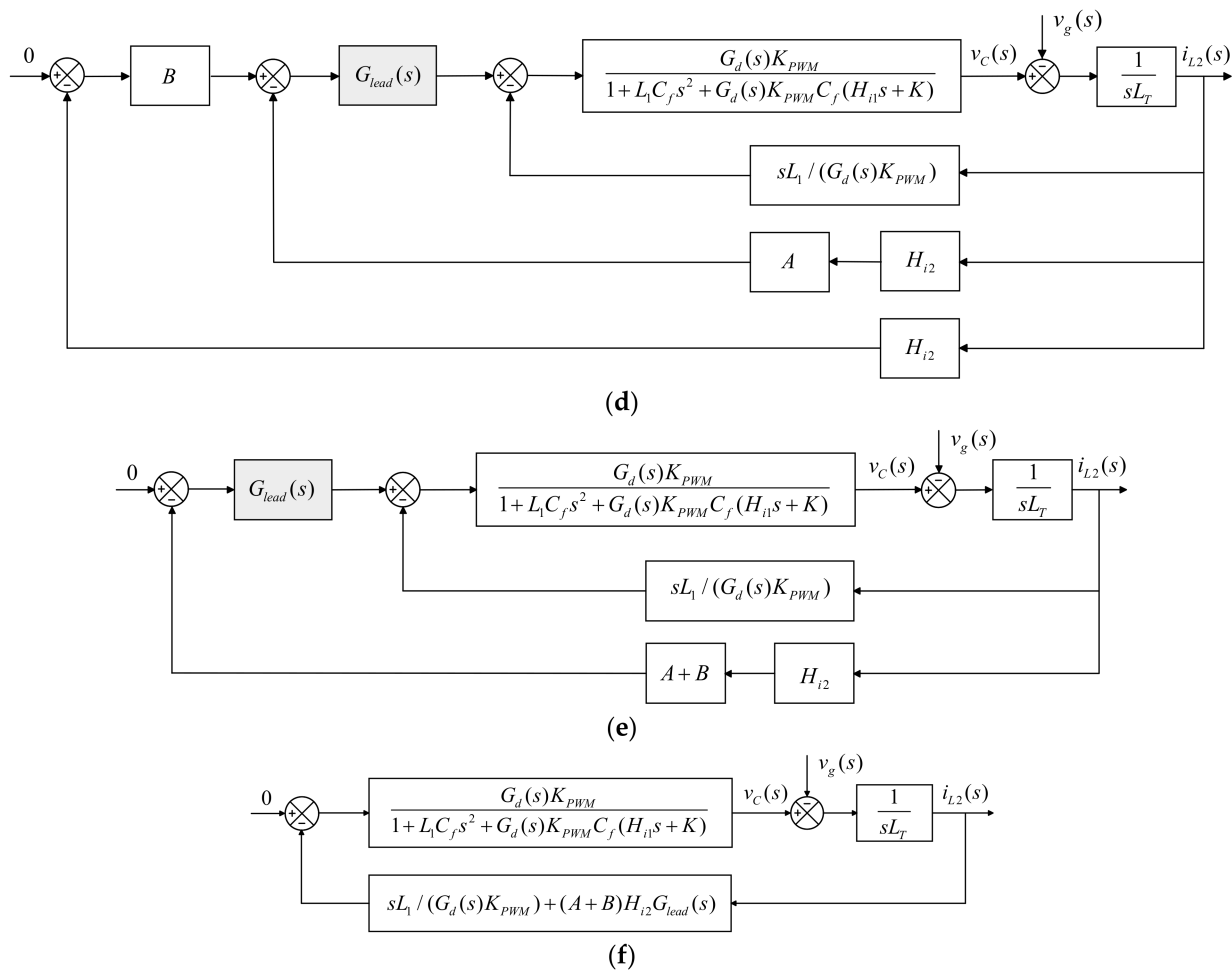


Figure A1. Equivalent block diagrams transformed from Figure 22, (a–f) show the simplification process of the control block diagram.

References

- Zou, C.; Liu, B.; Duan, S.; Li, R. Influence of Delay on System Stability and Delay Optimization of Grid-Connected Inverters with LCL Filter. *IEEE Trans. Ind. Inform.* **2014**, *10*, 1775–1784. [\[CrossRef\]](#)
- Liserre, M.; Teodorescu, R.; Blaabjerg, F. Stability of photovoltaic and wind turbine grid-connected inverters for a large set of grid impedance values. *IEEE Trans. Power Electron.* **2006**, *21*, 263–272. [\[CrossRef\]](#)
- Guan, Y.; Wang, Y.; Xie, Y.; Liang, Y.; Lin, A.; Wang, X. The Dual-Current Control Strategy of Grid-Connected Inverter with LCL Filter. *IEEE Trans. Power Electron.* **2019**, *34*, 5940–5952. [\[CrossRef\]](#)
- Yao, W.; Yang, Y.; Zhang, X.; Blaabjerg, F.; Loh, P.C. Design and Analysis of Robust Active Damping for LCL Filters Using Digital Notch Filters. *IEEE Trans. Power Electron.* **2017**, *32*, 2360–2375. [\[CrossRef\]](#)
- Xin, Z.; Wang, X.; Loh, P.C.; Blaabjerg, F. Grid-Current-Feedback Control for LCL-Filtered Grid Converters with Enhanced Stability. *IEEE Trans. Power Electron.* **2017**, *32*, 3216–3228. [\[CrossRef\]](#)
- Dannehl, J.; Liserre, M.; Fuchs, F.W. Filter-Based Active Damping of Voltage Source Converters with LCL Filter. *IEEE Trans. Ind. Electron.* **2011**, *58*, 3623–3633. [\[CrossRef\]](#)
- Yao, W.; Yang, Y.; Xu, Y.; Blaabjerg, F.; Liu, S.; Wilson, G. Phase Reshaping via All-Pass Filters for Robust LCL-Filter Active Damping. *IEEE Trans. Power Electron.* **2020**, *35*, 3114–3126. [\[CrossRef\]](#)
- Pan, D.; Ruan, X.; Bao, C.; Li, W.; Wang, X. Optimized Controller Design for LCL-Type Grid-Connected Inverter to Achieve High Robustness Against Grid-Impedance Variation. *IEEE Trans. Ind. Electron.* **2015**, *62*, 1537–1547. [\[CrossRef\]](#)
- Liu, T.; Liu, J.; Liu, Z.; Liu, Z. A Study of Virtual Resistor-Based Active Damping Alternatives for LCL Resonance in Grid-Connected Voltage Source Inverters. *IEEE Trans. Power Electron.* **2020**, *35*, 247–262. [\[CrossRef\]](#)
- Bao, C.; Ruan, X.; Wang, X.; Li, W.; Pan, D.; Weng, K. Step-by-Step Controller Design for LCL-Type Grid-Connected Inverter with Capacitor-Current-Feedback Active-Damping. *IEEE Trans. Power Electron.* **2014**, *29*, 1239–1253.
- He, Y.; Wang, X.; Ruan, X.; Pan, D.; Qin, K. Hybrid Active Damping Combining Capacitor Current Feedback and Point of Common Coupling Voltage Feedforward for LCL-Type Grid-Connected Inverter. *IEEE Trans. Power Electron.* **2020**, *36*, 2373–2383. [\[CrossRef\]](#)

12. Pan, D.; Ruan, X.; Bao, C.; Li, W.; Wang, X. Capacitor-Current-Feedback Active Damping with Reduced Computation Delay for Improving Robustness of LCL-Type Grid-Connected Inverter. *IEEE Trans. Power Electron.* **2014**, *29*, 3414–3427. [[CrossRef](#)]
13. Abady, I.M.; Amer, T.S.; Gad, H.M.; Bek, M.A. The asymptotic analysis and stability of 3DOF non-linear damped rigid body pendulum near resonance. *Ain Shams Eng. J.* **2022**, *13*, 2090–4479. [[CrossRef](#)]
14. Amer, W.S. The dynamical motion of a rolling cylinder and its stability analysis: Analytical and numerical investigation. *Arch. Appl. Mech.* **2022**, *92*, 3267–3293. [[CrossRef](#)]
15. Xin, Z.; Mattavelli, P.; Yao, W.; Yang, Y.; Blaabjerg, F.; Loh, P.C. Mitigation of Grid-Current Distortion for LCL-Filtered Voltage-Source Inverter with Inverter-Current Feedback Control. *IEEE Trans. Power Electron.* **2018**, *33*, 6248–6261. [[CrossRef](#)]
16. Liserre, M.; Teodorescu, R.; Blaabjerg, F. Multiple harmonics control for three-phase grid converter systems with the use of PI-RES current controller in a rotating frame. *IEEE Trans. Power Electron.* **2006**, *21*, 836–841. [[CrossRef](#)]
17. Xiao, P.; Corzine, K.A.; Venayagamoorthy, G.K. Multiple Reference Frame-Based Control of Three-Phase PWM Boost Rectifiers under Unbalanced and Distorted Input Conditions. *IEEE Trans. Power Electron.* **2008**, *23*, 2006–2017. [[CrossRef](#)]
18. Mohamed, Y.A. Suppression of Low- and High-Frequency Instabilities and Grid-Induced Disturbances in Distributed Generation Inverters. *IEEE Trans. Power Electron.* **2011**, *26*, 3790–3803. [[CrossRef](#)]
19. Wang, X.; Ruan, X.; Liu, S.; Tse, C.K. Full Feedforward of Grid Voltage for Grid-Connected Inverter with LCL Filter to Suppress Current Distortion Due to Grid Voltage Harmonics. *IEEE Trans. Power Electron.* **2010**, *25*, 3119–3127. [[CrossRef](#)]
20. Li, W.; Ruan, X.; Pan, D.; Wang, X. Full-Feedforward Schemes of Grid Voltages for a Three-Phase LCL-Type Grid-Connected Inverter. *IEEE Trans. Ind. Electron.* **2013**, *60*, 2237–2250. [[CrossRef](#)]
21. Abeyasekera, T.; Johnson, C.M.; Atkinson, D.J.; Armstrong, M. Suppression of Line Voltage Related Distortion in Current Controlled Grid Connected Inverters. *IEEE Trans. Power Electron.* **2005**, *20*, 1393–1401. [[CrossRef](#)]
22. Zhao, R.; Li, Q.; Xu, H.; Wang, Y.; Guerrero, J.M. Harmonic Current Suppression Strategy for Grid-Connected PWM Converters with LCL Filters. *IEEE Access* **2019**, *7*, 16264–16273. [[CrossRef](#)]
23. Wang, X.; Blaabjerg, F.; Loh, P.C. Virtual RC Damping of LCL-Filtered Voltage Source Converters with Extended Selective Harmonic Compensation. *IEEE Trans. Power Electron.* **2015**, *30*, 4726–4737. [[CrossRef](#)]
24. He, Y.; Wang, X.; Ruan, X.; Pan, D.; Xu, X.; Liu, F. Capacitor-Current Proportional-Integral Positive Feedback Active Damping for LCL-Type Grid-Connected Inverter to Achieve High Robustness Against Grid Impedance Variation. *IEEE Trans. Power Electron.* **2019**, *34*, 12423–12436. [[CrossRef](#)]
25. Yoon, C.; Bai, H.; Beres, R.N.; Wang, X.; Bak, C.L.; Blaabjerg, F. Harmonic Stability Assessment for Multiparalleled, Grid-Connected Inverters. *IEEE Trans. Sustain. Energy* **2016**, *7*, 1388–1397. [[CrossRef](#)]
26. Wang, X.; He, Y.; Pan, D.; Zhang, H.; Ma, Y.; Ruan, X. Passivity Enhancement for LCL-Filtered Inverter with Grid Current Control and Capacitor Current Active Damping. *IEEE Trans. Power Electron.* **2022**, *37*, 3801–3812. [[CrossRef](#)]
27. Awal, M.A.; Yu, W.; Husain, I. Passivity-Based Predictive-Resonant Current Control for Resonance Damping in LCL-Equipped VSCs. *IEEE Trans. Ind. Appl.* **2020**, *56*, 1702–1713. [[CrossRef](#)]
28. Wang, X.; Blaabjerg, F.; Loh, P.C. Passivity-Based Stability Analysis and Damping Injection for Multiparalleled VSCs with LCL Filters. *IEEE Trans. Power Electron.* **2017**, *32*, 8922–8935. [[CrossRef](#)]
29. Harnefors, L.; Zhang, L.; Bongiorno, M. Frequency-domain passivity-based current controller design. *IET Power Electron.* **2008**, *1*, 455–465. [[CrossRef](#)]
30. Xin, Z.; Wang, X.; Loh, P.C.; Blaabjerg, F. Realization of Digital Differentiator Using Generalized Integrator for Power Converters. *IEEE Trans. Power Electron.* **2015**, *30*, 6520–6523. [[CrossRef](#)]
31. Xin, Z.; Loh, P.C.; Wang, X.; Blaabjerg, F.; Tang, Y. Highly Accurate Derivatives for LCL-Filtered Grid Converter with Capacitor Voltage Active Damping. *IEEE Trans. Power Electron.* **2016**, *31*, 3612–3625. [[CrossRef](#)]
32. Pan, D.; Ruan, X.; Wang, X. Direct Realization of Digital Differentiators in Discrete Domain for Active Damping of LCL-Type Grid-Connected Inverter. *IEEE Trans. Power Electron.* **2018**, *33*, 8461–8473. [[CrossRef](#)]
33. Yepes, A.G.; Freijedo, F.D.; Lopez, Ó.; Doval-Gandoy, J. High-Performance Digital Resonant Controllers Implemented with Two Integrators. *IEEE Trans. Power Electron.* **2011**, *26*, 563–576. [[CrossRef](#)]
34. IEEE Standard 1547-2018 (Revision of IEEE Standard 1547-2003); IEEE Standard for Interconnection and Interoperability of Distributed Energy Resources with Associated Electric Power Systems Interfaces. IEEE: Piscataway, NJ, USA, 2018; pp. 1–138.
35. Xu, J.; Xie, S.; Tang, T. Evaluations of current control in weak grid case for grid-connected LCL-filtered inverter. *IET Power Electron.* **2013**, *6*, 227–234. [[CrossRef](#)]
36. Chen, X.; Ruan, X.; Yang, D.; Zhao, W.; Jia, L. Injected Grid Current Quality Improvement for a Voltage-Controlled Grid-Connected Inverter. *IEEE Trans. Power Electron.* **2018**, *33*, 1247–1258. [[CrossRef](#)]
37. He, Y.; Wang, X.; Pan, D.; Ruan, X.; Su, G. An Ignored Culprit of Harmonic Oscillation in LCL-Type Grid-Connected Inverter: Resonant Pole Cancellation. *IEEE Trans. Power Electron.* **2021**, *36*, 14282–14294. [[CrossRef](#)]